Tuning the CO_2 Reduction Selectivity by Controllable Silver Plating on Copper Nano-catalysts

By

Fei Xu

A thesis submitted to Johns Hopkins University in conformity with the requirements

for the degree of Master of Science

Baltimore, Maryland

May 2018

Abstract

With drastically increasing consumption of fossil fuels in industries and transportations, the emission of carbon dioxide (CO_2), a green-house gas, has become a major contributor to global warming. As a result, a renewable CO_2 reduction scheme has become urgent for a sustainable future.

An ideal solution to address this problem is the electrochemical reduction of carbon dioxide to fuels or other valuable products through the use of sustainable energy (such as wind, solar, hydro, etc.). However, researchers have found this solution challenging due to a lack of known catalysts with high activity and selectivity for CO_2 reduction.

The work performed within this thesis reports a novel method to successfully synthesize and control Cu@Ag core-shell nanoparticles with different mass ratios of Silver/Copper alloy shells, and their application as electro-catalysts for carbon dioxide electro-reduction. The catalytic results revealed the structure-property relationships. The different silver mass ratios lead to different synergistic effects, which significantly increases the selectivity of CO_2 electro-reduction.

Acknowledgements

I would first thank my advisor, Dr. Chao Wang. It has been my pleasure to be his Master's student, and PhD student in the coming semester. He did not only teach me electrochemistry and nanoparticle technologies, he also taught me the cautious scientific attitude. His enthusiasm and unremittingness for research was very simulative. I appreciate all his contributions of time, ideas and financial support to make me finish these projects.

Next person I would like to give a specific appreciation is Dr. Lei Wang, whom I worked with during these two years. He is a great source of friendship, advice and collaboration. I would like to express my deepest gratitude to him. The other members of the Wang Lab have also provided me abundant helps. I would like to thank Danyan Zhang, the undergraduate student working with me for her hard working on synthesis experiment. Also, I would like to thank Dr. David Raciti and Yuxuan Wang for advising me doing CO_2 reduction experiments.

Lastly, I would like to thank my love ones for all their love, financial support, and encouragement they provided me in completing the Master's degree.

Contents

Table of Figures and Tables:

1 Introduction

1.1. Motivation

The purpose behind the work presented in this thesis is to develop and understand the structure of nanoscale materials and their applications for solving global energy issues. The research within these projects relied on the meticulously designed nanomaterials structures. We combined the study of nano-material synthesis and electro-chemical catalytic reactions to seek the link between the material structure and catalytic activity.

This thesis presents the synthesis of Cu/Ag alloy core-shell nanoparticles as an electro-catalyst for the CO_2 reduction reaction. In this work, we successfully control the mass ratio of silver/copper metal, comprehensively evaluate the electro-catalytic performance of silver/copper alloy nanoparticles and correlate the results to precise nanostructures characterized by Transmission Electron Microscopy (TEM), Inductively Coupled Plasma Mass Spectrometry (ICP-MS), X-ray Diffraction (XRD), and X-ray Photoelectron Spectroscopy (XPS).

The remainder of this introduction is introducing the theory and techniques behind controlling nanoparticle synthesis and the fundamentals of the electro-reduction of CO_2.

1.2. Fundamentals of Nanoparticle Synthesis

By definition, nanomaterials have micro structures on the nanometer scale (100 nm) range, and furthermore show unique properties from their bulk materials. In recent years nanoparticles

have attracted extensive attention due to the enormous changes in the physical and chemical properties of new materials, arising from the transition from micro-scale materials to Nano-scale materials[1]. It is well documented that the decreasing size at the nano-scale significantly increases the surface area of the material and gives rise to new properties. Nanoparticles can be classified as single, core-shell or composite nanoparticles depending on the composition of the material[1]. Typically, single nanoparticles consist of only one material; alternatively, the composite and core-shell particles are composed of two or more materials. Bimetallic nanoparticles are much more interesting than single metallic nanoparticles because of their unique properties arising from synergistic or lattice strain effects between the two metals.

Core-shell nanoparticles have been extensively studied by researchers as these nanoparticles have intriguing potential in electronics, biomedicine, pharmaceuticals, optics and catalysis. Core-shell nanoparticles are highly functional materials with improved properties[2]. The properties of these nanoparticles endowed by both metal materials can be integrated precisely, resulting in highly functional materials with a tunable composition. These properties can be easily changed by replacing the constituent materials or the bimetallic ratio. Ultimately, the particles show exclusive properties stemming from the diverse materials used together. The purpose of bimetallic particles concentrates on surface modification, contributing to a variety of functionality, stability, dispersion, and reduction properties of the valuable materials[1,3]. Additionally, composite nanoparticles are also brilliant from the perspective of eco-friendly materials. When a noble metal and non-noble metal are combined, the catalytic performance is enhanced and modified at a lower consumption of precious metal compared with pure noble

materials of the same size.[2-4]

Methods of core-shell nanoparticles preparation are broadly divided into "top down" and "bottom up" synthesis methods[5]. The "top down" approach typically uses a conventional physical operation such as cutting, polishing, and chipping particles into an ideal shape using external force from tools. For instance, most of the techniques are electron/ion beam, scanning probe, or laser beam processing, and other mechanical techniques. In contrast, the "bottom up" method utilizes the natural properties of molecules to assemble themselves by advantageous formation. The widest used measures of “bottom up” are thermal synthesis, chemical vapor deposition, laser-tapping, etc. However, both the “top down” and “bottom up” methods are critical to establishing distinguished properties. In general, we can obtain size controlled particles through a “bottom up” method, which can also produce nanoparticles in smaller size compared with the “top down” method. Furthermore the “bottom up” method may become more cost effective in future applications due to the strengths of absolute accuracy and complete control procession, as well minimal energic consumption when compared to the “top down” method[1]. It is also feasible to use a combination of two methods. In our project, the “bottom up” approach is more applicable in synthesizing copper/silver alloy core-shell nanoparticles.

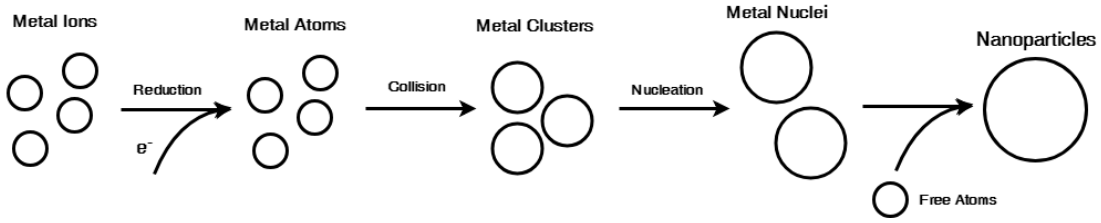

Figure 1-1 General mechanism of nanoparticle synthesis in organic solutions

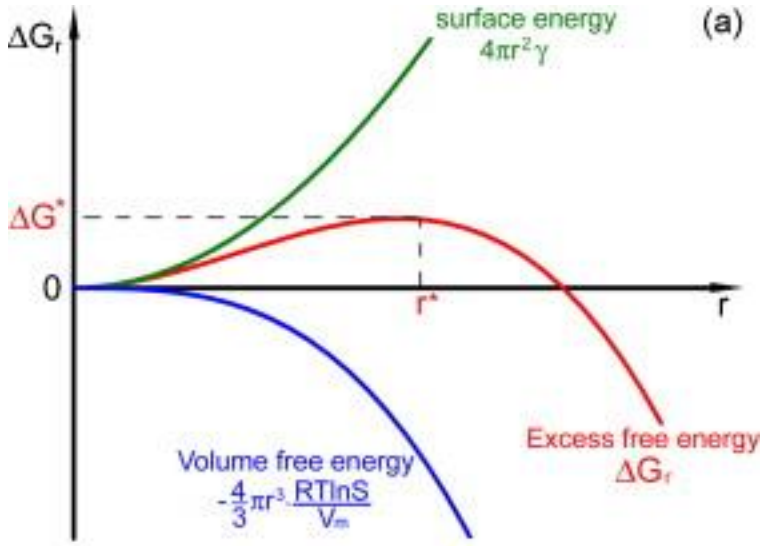

Figure 1-2 Overall excess free energy as a function of cluster size. Source: Peng, Z. M. & Yang, H. Designer platinum nanoparticles: Control of shape, composition in alloy, nanostructure and electrocatalytic property. *Nano Today* **4**, 143-164 (2009).[6]

Fig. 1-1 is showing the general mechanism of nanoparticle synthesis in organic solution. Also, Fig. 1-2 is showing the relationship between overall excess free energy with the size of nanoparticles. The nucleation process is an Ostwald ripening process. At initial stages, the metal atoms form through the reduction of metal ions. The overall free energy is at the lowest stage. Then these metal atoms collide with each other to produce small clusters that are thermodynamically unstable, so the free energy starts to increase. After the clusters overcome a critical free energy barrier (G*) and become thermodynamically stable nuclei. These nuclei grow into nanoparticles at the consumption of free atoms in solution or unstable small clusters. After reaching the critical radius, the nanoparticles are hard to combine more atoms. The smaller cluster will consume the rest free atoms, so the overall systematic free energy will decrease.

1.3. Galvanic Replacement

The galvanic replacement reaction has become an attractive method for the synthesis of bimetallic nanomaterials during the past decade[7]. Compared with other methods, it enables a single reaction step to control the morphology and size as well the surface composition of nanoparticles[8]. Typically, galvanic replacement involves an erosion process which results from different electronic potentials between two metals and the products are generally proven to have excellent performance in catalytic applications.

Commonly the galvanic replacement reaction consists of a redox reaction in a solid metal as a template and the other metal as ions for shell or hollow materials[9]. The force of the reaction can be qualified as two simultaneous reactions: oxidation-corrosion of the solid template (base) and reduction-deposition of another metal. (Metal ions in solution are reduced first, subsequently accompanied with a precipitation reaction on the surface of metal template.) In this way, researchers can control the size and morphology by adjusting the ratio of the solid template to the metal ions and the original geometry of the solid template. This approach contributes to the diversity of nanoparticles from both template and metal ions combinations, such as alloys, core-shell, tubes, wires, and frames.

In the past decade, galvanic replacement reaction has been widely used in the synthesis of bimetallic nanomaterials with great efficiency and versatility[10]. The control of temperature in a replacement reaction is perhaps the most crucial element. Temperature has a great influence on both solid base as well as metal ions. Primarily, temperature effects the diffusion rate of ions

in solution, as well as the relative formation and deposition of the metal nanoparticles. Normally, increasing the temperature results in lower reaction kinetics for exothermic reactions and vice versa for endothermic reactions. In the process of formation and deposition (precipitation), temperature serves three purposes: nucleation, growth, and agglomeration. The temperature of nucleation depends on the chemical itself. In contrast, the growth process is totally influenced by temperature and results from the impact on diffusion rates. The diffusion of metal atoms from bulk to the metal surface accelerates with increasing temperature. For endothermic reactions, higher temperature leads to an increasing concentration of product in the bulk, resulting in a higher diffusion rate and ending in higher reaction speeds. At the same time, higher temperature leads to a negative trend in reaction speed because of a decreasing concentration of products in the bulk. In general, when synthesizing a core-shell nanoparticle, a lower temperature is favorable because it will maximize the concentration of additive material ions that are unsaturated in the complex[11].

1.4. Synergistic Effect

This study shows that the synergistic effect on the performance of different metal nano-catalysts is majorly impacted by the surface state of the electrons[12,13]. The electronic state of the surface is greatly influenced by changes in the geometric parameters of the catalyst, and it is also closely related to the local lattice strain and the number of effective atom coordination planes. These new bimetallic catalysts have attracted scholars' research enthusiasm in recent years due to new exciting applications such as fuel cells for efficient energy conversion from

renewable resources[14]. In the past few years, this field has obtained much more attention due to the huge demand of high-performance catalysts in industrial production[15]. Specifically, the usage of Ni, Fe, Cu, and other NPs and precious metals can reduce the amount of expensive noble metals in use, and in that way reducing the cost of the catalyst.

Researchers around the world have made great progress in the preparation of bimetallic nanoparticles with the synergistic effect, and have already achieved some good results. Experimental studies of these bimetallic alloy nanoparticles have demonstrated efficient catalytic synergy in related reactions such as methanol fuel cells, electrochemical oxidation of ethanol and formic acid, carbon monoxide oxidation, and oxygen reduction chemical storage systems. In addition, due to the synergistic effect between the metals, the performance of the bimetallic nano analyzer is better than that of a single metal[14]. Researchers from Berkeley have found that the gold-copper bimetallic nanoparticles with synergistic geometry showed significantly higher selectivity and activity when compared with gold or copper nanoparticles[16].

1.5. Greenhouse Gas Effect of CO_2

Carbon Dioxide (CO_2) is an important green-house gas, which absorbs heat. Earth's surface land and ocean assimilate radial thermal energy uninterruptedly[17]. Unlike oxygen or nitrogen, the major contents of Earth's atmosphere, greenhouse gases captivate the heat and release it slowly over time. Carbon dioxide is more abundant and lasts longer than other greenhouse gases, so it causes much more sever global environmental issues. On the other hand, carbon dioxide could react with water molecules and produce carbonic acid, which reduces the

pH of ocean water. The acidification of ocean water decreases the ability of many marine organisms to build their shells and skeletal structures[18]. The predominant source of CO_2 is the combustion of hydrocarbon fossil fuels, which is the major technique for energy production[19]. In 2016, United States produced about 97.4 quadrillion British thermal units (BTUs), 81% coming from hydrocarbon fossil fuels combustion (Fig. 1-1).

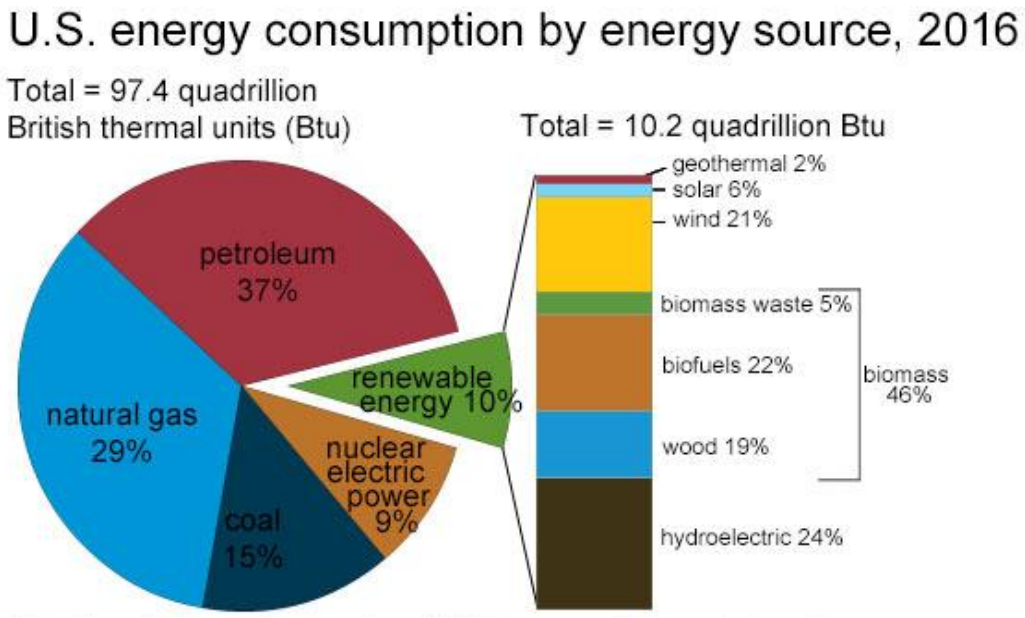

Figure 1-3 U.S. energy consumption by energy sources in 2016. Source: U.S. Energy Information Administration, Monthly Energy Review, Table 1.3 and 10.1, April 2017, preliminary data[19,20]

According to the data from NASA, the current global average atmospheric carbon dioxide level reached 400 ppm, which is higher than any point in at least the past 800,000 years[21]. In the past 100 years, the CO_2 concentration level has increased 1.5-fold from 290 ppm to 400 ppm[22] (Fig. 1-2). In the meantime, the global average temperature has increased as well, which is related to greenhouse gas effect of carbon dioxide. In the past 100 years, the mean global

temperature increased by 0.9 °C[23] (Fig. 1-3). Increasing CO_2 concentrations have not only increased global temperature, but also resulted in other severe environmental issues as well. The arctic sea ice reaches its minimum level each September; according to NASA's data, from 1981 to 2010, the sea ice is declining at a rate of 13.2 percent per decade. In addition, in 2012 the sea ice reached the lowest level on record[24] (Fig. 1-4). The data from NASA also showed that the land ice sheets in both Antarctica and Greenland have been losing mass since 2002[25] (Fig. 1-5). Moreover, the sea level is rising due to the added water from melting ice sheets and glaciers, and water expansion as it warms. Fig. 1-6 shows the sea level change since 1993' an average increase of 3.2 millimeters per year is observed[26].

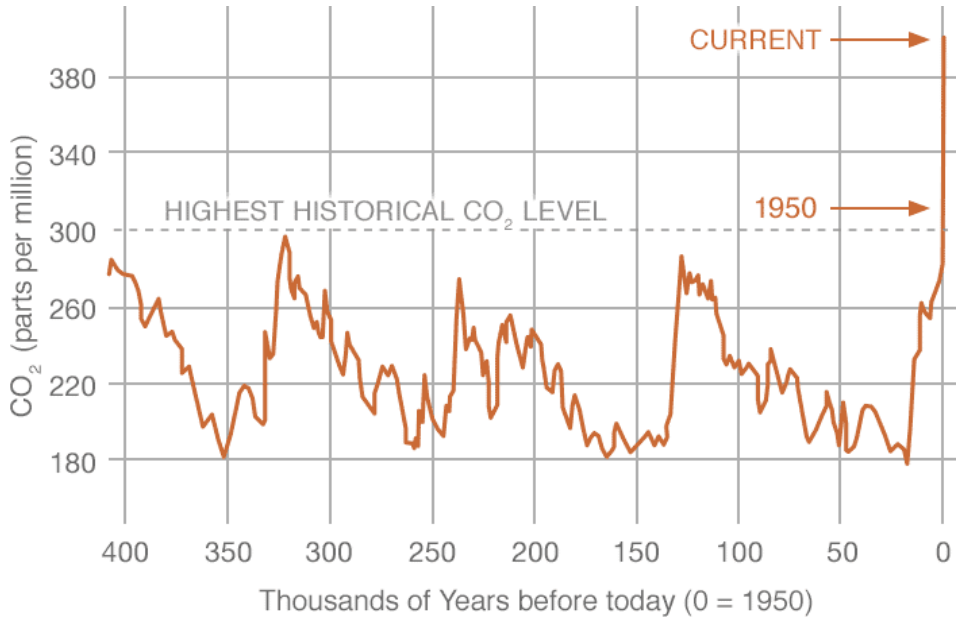

Figure 1-4 Atmospheric Carbon Dioxide level in the past 400,000 years. Source: "Carbon Dioxide", Earth Science Communications Team at NASA's Jet Propulsion Laboratory. https://climate.nasa.gov/vital-signs/carbon-dioxide/[22]

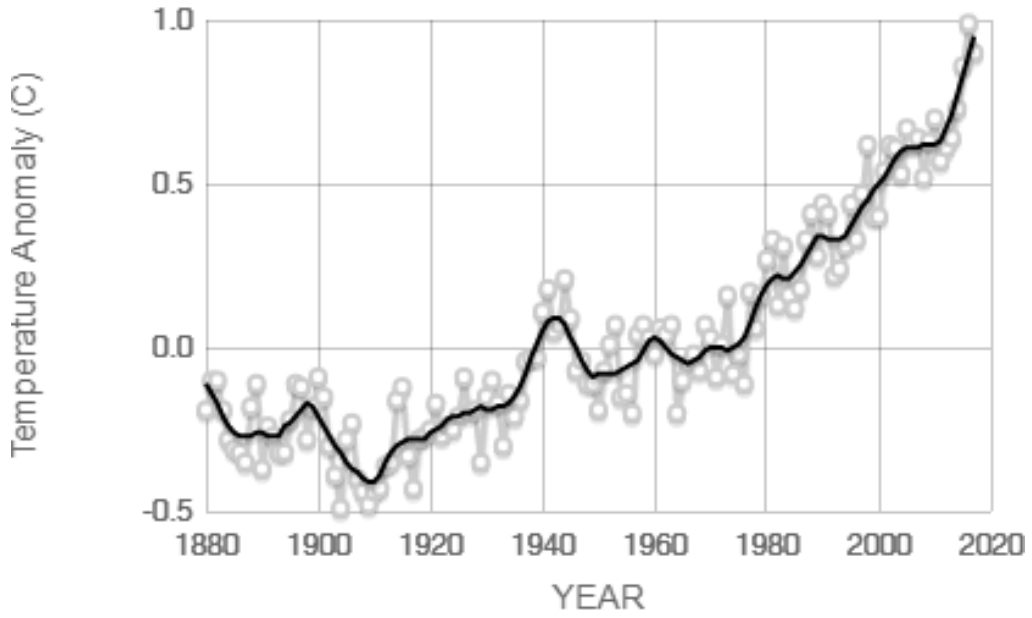

Figure 1-5 Global temperature changes during the past 140 years. Source: "Global Temperature", Earth Science Communications Team at NASA's Jet Propulsion Laboratory. https://climate.nasa.gov/vital-signs/global-temperature/[23]

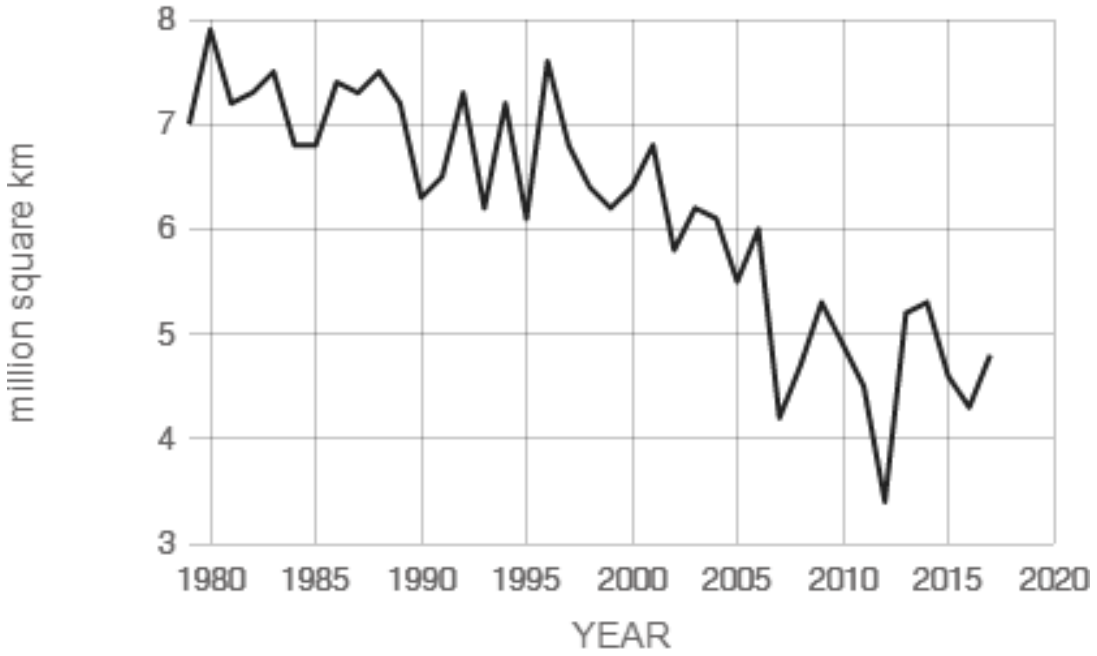

Figure 1-6 Arctic sea ice level in the past 40 years. It reaches the lowest at 2012 in the record. Source: "Arctic Sea Ice Minimum", Earth Science Communications Team at NASA's Jet Propulsion Laboratory.

https://climate.nasa.gov/vital-signs/arctic-sea-ice/[24]

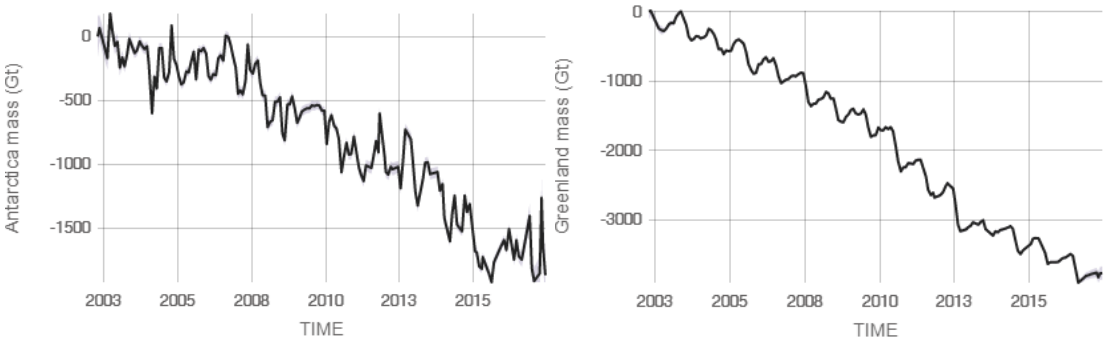

Figure 1-7 The ice sheets mass of Antarctica and Greenland from 2002. Source: "Ice Sheets", Earth Science Communications Team at NASA's Jet Propulsion Laboratory. https://climate.nasa.gov/vital-signs/ice-sheets/[25]

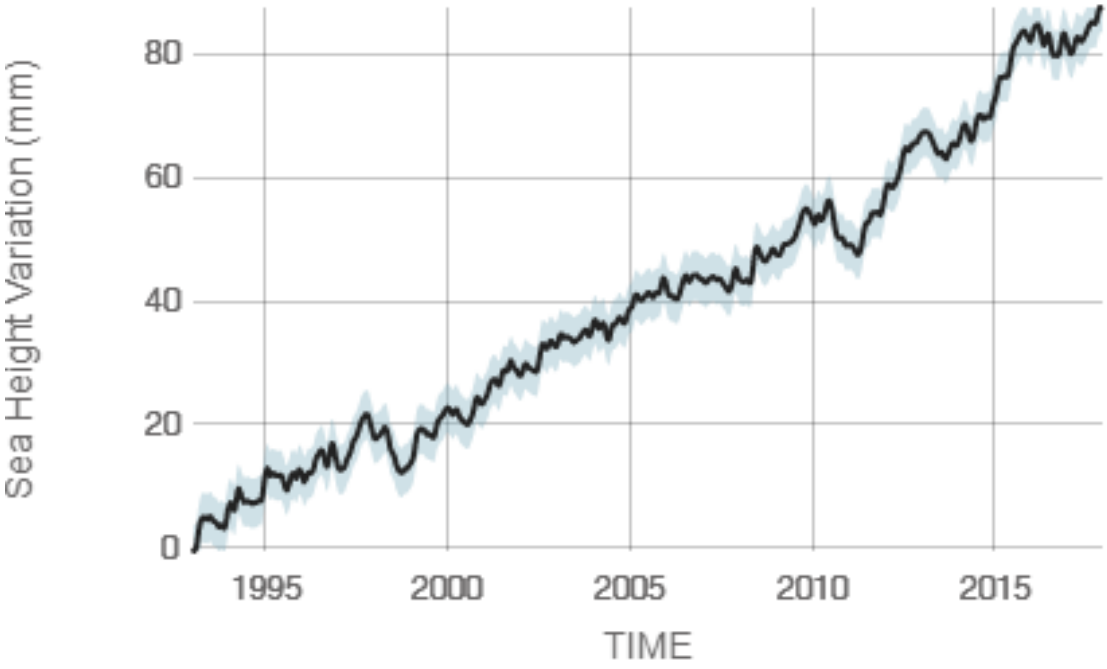

Figure 1-8 The sea level has increased 3.2 millimeters per year since 1993. Source: "Ice Sheets", Earth Science Communications Team at NASA's Jet Propulsion Laboratory. https://climate.nasa.gov/vital-signs/sea-level/[26]

1.6. CO_2 Electrochemical Reduction

Addressing this issue, plenty of solutions have been proposed and he study of new

alternative sustainable energy technologies has attracted much attention. However, reducing the emission of carbon dioxide from substitute sustainable energy (such as wind, solar, hydro, etc.) is not an impressive solution. Because of the high cost and immature technology, renewable energy is not being widely employed. A promising solution to address the CO_2 problem is converting them to fuels or other valuable products.

Various methods have been reported during the past few decades[5] where electrochemical carbon dioxide reduction has received surprising consideration from a point of both efficiency and economic advantages. Catalysts used in carbon dioxide reduction are reusable, resulting in minimal consumption of chemicals. Furthermore, electrochemical conversion of carbon dioxide is differentiable from any other thermochemical conversion method because they can be used at ambient temperature and pressure[9]. Subsequently, a serious of metal catalysts have been tried on carbon dioxide reduction to optimize the selectivity and efficiency of products[27-30].

The direct combination method of different metals and carbon dioxide results in the selectivity of different metals to the product. More economical catalysts like copper have been demonstrated to produce 18 different products in CO_2 reduction reaction[31,32]. Fig. 1-7 show the numbers of electrons transferred for the most common products in CO_2 electro-reduction reaction and their prices.

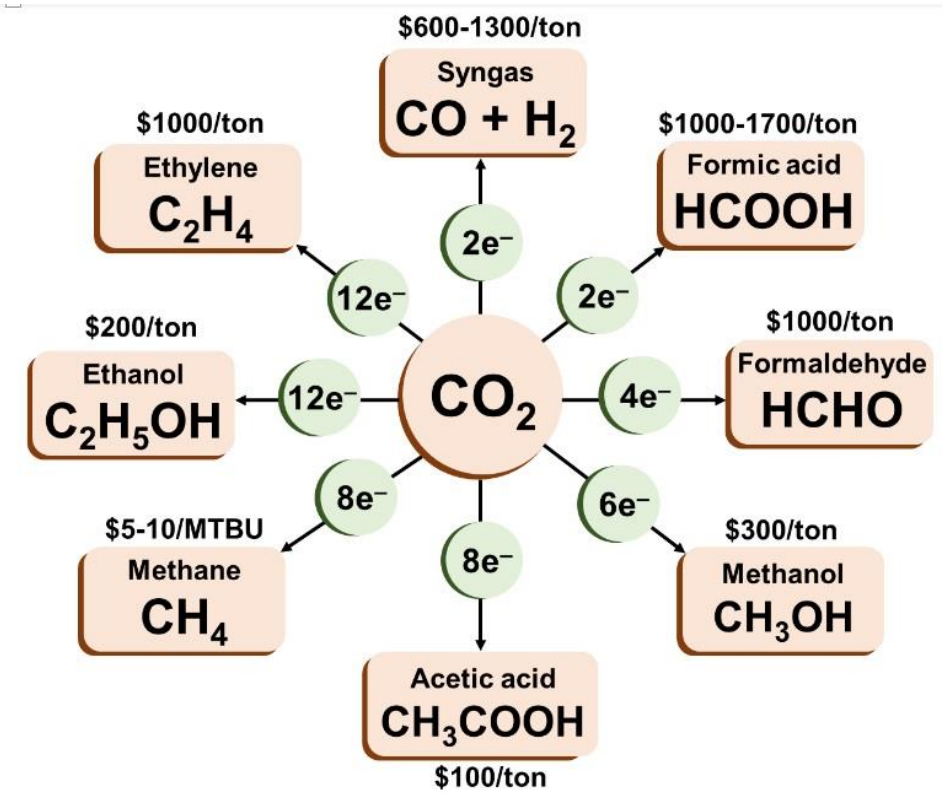

Figure 1-9 CO2 electrochemical-reduction products and their market prices. Sources: "CO2 to fuels", Irina Chernyshova. http://blogs.cuit.columbia.edu/ic2228/co2-to-fuels/[33]

Generally, the products can be classified into 3 groups: formic acid, higher products (alcohol, methanol, hydrocarbon, etc.)[10], and CO resulting from different types of metal catalysts. The first group is non-coordinating and non-reducing CO, in which formic acid is the primary product. In contrast, the remaining two groups can combine with CO2•- and produce CO. However, the two groups can continue to be separated by their ability in the further reduction of CO. Those that can continue to react the CO reduction (the third group) finally obtain higher products (such as alcohol, hydrocarbon, etc.) while another gets CO as main product[11].

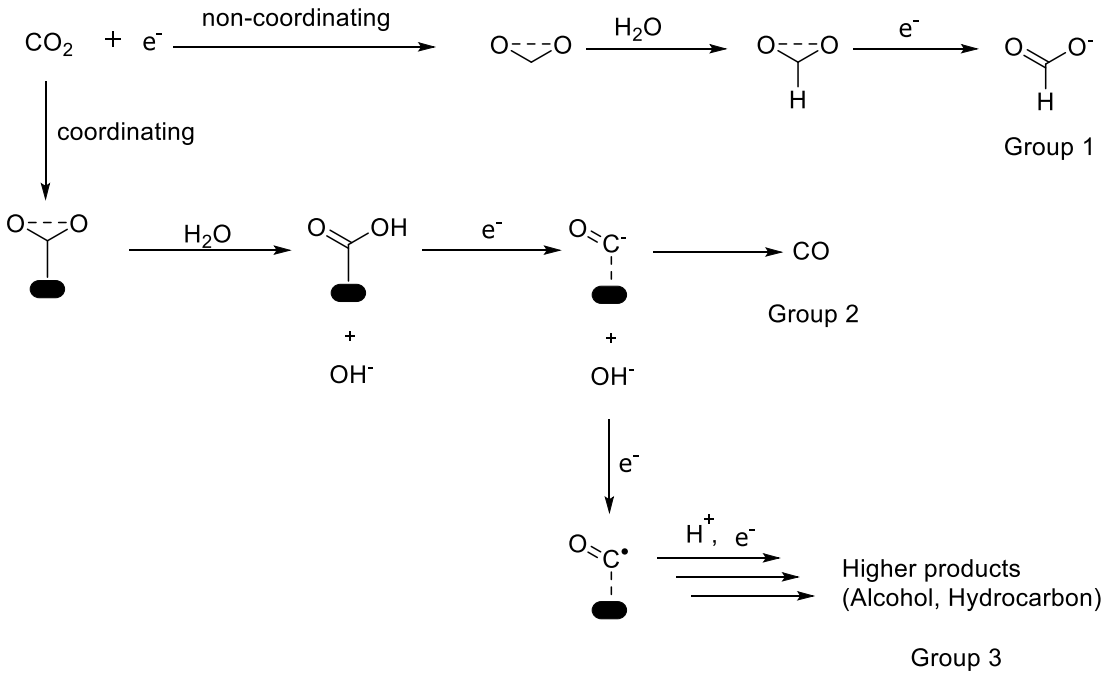

Figure 1-10 Mechanisms of CO2 electrochemical-reduction reactions. The first group of products is formic acid. Second group of products is carbon monoxide. And the third group of products is hydrocarbons with more carbon atoms.

Among the catalysts performance, the production of $CO_2^{\bullet-}$ is crucial because it is the rate-limiting step, meanwhile the coordination of this intermediate determines whether the $2e^-$ reduction is CO or formic acid. Compared with the rate-limiting step, the subsequent reduction steps are almost instantaneous. Notably, $CO_2^{\bullet-}$ shows a high energy and good performance to react with H_2O and any other molecules in aqueous environments. From a previous report, the stabilization of a high energy intermediate is the key to achieving a high-speed and energy-efficient CO_2 reduction process[34].

The three main products of CO_2 reduction are hydrogen, carbon monoxide, and formic acid. The following equations show the reactions for these products and their equilibrium

potentials (vs. SHE).

$$2\mathrm{H}^+ + 2e^- \rightarrow H_2 \quad E_0 = 0.000\,V$$

$$2\mathrm{CO}_2 + 8H^+ + 2e^- \rightarrow CO + H_2O \quad E_0 = 0.169\,V$$

$$\mathrm{CO}_2 + H^+ + e^- \rightarrow HCOO^- + H_2O \quad E_0 = -0.225\,V$$

However, in the practical experiment, the formation of CO_2 reduction products always occurs at several hundreds of millivolts below their potential due to sluggish kinetics.

Generally, the CO_2 reduction reaction is possessed in aqueous solutions, with an additional hydrogen evolution reaction (HER) occurring synchronously, which plays a vital effect on the selectivity of products. In addition, the most expecting product of electrochemical reduction usually is CO, which has a more simple mechanism than any other product due to it is a two-electron reduction reaction[34]. Furthermore, CO can be an impressive product not only as a kind of feedstock chemical but also because it is easy to extract from systems as a gas when compared with other products (methanol, alcohol, formic acid, etc.).

The efficiency of the CO_2 electrochemical reduction is described as the faradaic efficiency (FE) of the reaction. FE is the percentage of electrons consumed by desirable products, otherwise known as "selectivity"[34]. FE can be easily calculated by counting the number of electrons which go through the reaction systems and comparing the electrons used for producing target products.

2 Experimental Methods

2.1. Synthesis

Chemicals. Copper (II) acetylacetonate ($Cu(acac)_2$), oleyl amine (OAm), 1,2-Dichlorobenzene (DCB), and Borane tert-butylamine (BTB) was purchased from Sigma Aldrich, and Silver Nitrate ($AgNO_3$) was purchased from Strem Chemicals Inc.

For bimetallic alloy nanoparticles, a reduction reaction of metallic salts is direct and convenient for both base and additive metal synthesis. As for reaction systems, a non-aqueous phase with surfactants and proper reducing agents for respective metals are necessary[34]. Reducing agents are critical for synthesis in different metal salts causes they restrain the galvanic replacement, and they always control both reaction rate and nanoparticle sizes altogether. Conventional reducing agents for metallic are sodium borohydride and hydrazine. Sodium borohydride is broadly used in either aqueous or non-aqueous solvent, and at any pH. While hydrazine is a stronger reducing agent, which is suitable for metallic salts with higher reduction potential respectively.

Additively, compared with typical reduction method, redox-trans-metalation is much more advanced. Take Cu-Ag system as a sample, with copper acetylacetone and silver nitrate are the metal precursors respectively, when silver nitrate diffuses to contact with the copper base on the surface, subsequently accompanied with redox reaction. The reducing agent prevented the copper base complete erosion by silver nitrate replacement reaction. When later injected silver nitrate diffused to the surface of copper base nanoparticles, the redox reaction is

taking placed. The copper metal is oxidized back to ion state and replaced by silver metal deposition. Once reached limit redox reaction potentials between copper and silver, the trans-metalation is a spontaneously process[35].

The chemical equation of reduction-transmetalation of bimetallic alloy particles can be represented as:

Cu base formation: $Cu^{2+} + 2e^{-} \rightarrow Cu \downarrow$

Ag additive formation: $Cu + 2Ag^{+} \rightarrow Cu^{2+} + 2Ag \downarrow$

Whereas, principles of synthesis alloy nanoparticles can be recognized as restricted galvanic replacement reaction.

2.1.1. Ag Nanoparticles

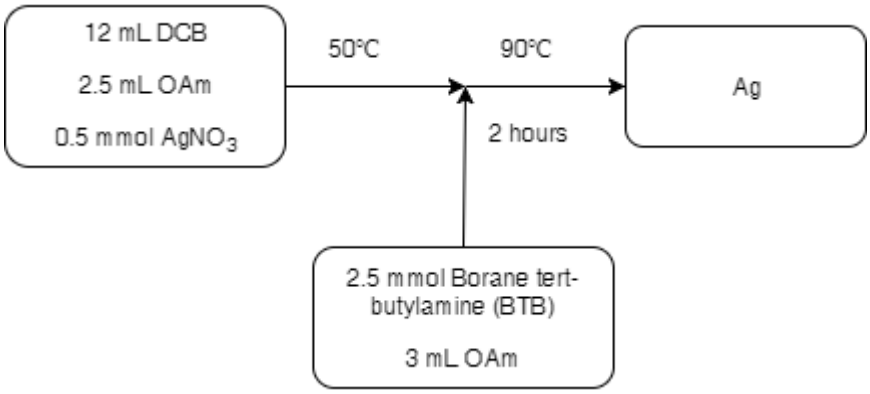

Figure 2-1 Schematic illustration of the synthetic route for Silver nanoparticles

Silver Nitrate (84.94 mg, 0.5 mmol), Dichlorobenzene (12 mLs) and Oleyl amine (5 mLs) was loaded into a glass three neck flask with a schlenk line setup under constant stirring. The resulting mixture was heated to 50℃ while purging with Argon gas, at which the outlet was

adjusted to a slight opening position to control the gas flowing at 1~2 bubbles per second. At mean time, Borane tert-butylamine (BTB) (182.85 mg, 2.5 mmol) was dissolved and ultra-sonicated in Oleyl amine (3 mLs). Then the flask gas outlet was closed to prevent the solvent from evaporating off, and the BTB solution was injected, and the solution was heated to 90℃ for 2 hours. A significant color change from clear to a deep yellow occurred after BTB injection. After re-open the gas outlet, the solution was cooled down to room temperature. Then the solution was diluted with ethanol to 50 mL and centrifuged at 8000 RPM for 10 minutes to precipitate out the copper nanoparticles from solution. The nanoparticles were then re-dispersed in 10 mL hexane.

2.1.2. Cu@Ag Nanoparticles

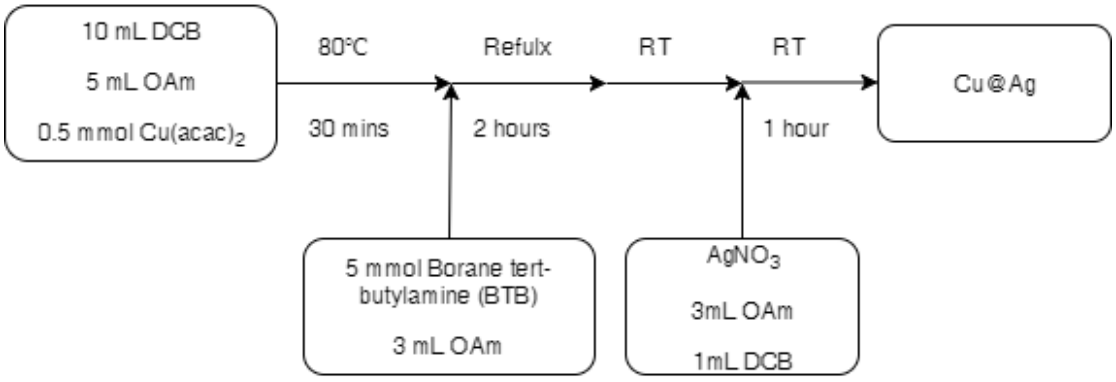

Figure 2-2 Schematic illustration of the synthetic route for Silver/Copper alloy nanoparticles

Three kinds of Copper/Silver alloy nanoparticles with different silver shell thickness were synthesized following the same route. Copper acetylacetonate (130 mg, 0.5 mmol), Dichlorobenzene (10 mLs) and Oleyl amine (5 mLs) was loaded into a glass three neck flask

with a schlenk line setup under constant stirring. The resulting mixture was heated to 80℃ while purging with Argon gas, at which the outlet was adjusted to a slight opening position to control the gas flowing at 1~2 bubbles per second. This solution was allowed to react for 30 minutes. At mean time, Borane tert-butylamine (BTB) (365.7 mg, 5 mmol) was dissolved and ultra-sonicated in Oleyl amine (5 mLs). Then the flask gas outlet was closed to prevent the solvent from evaporating off, and the BTB solution was injected, and the solution was heated to reflux for 2 hours. A significant color change from clear/yellow to a deep red occurred after BTB injection. After re-open the gas outlet, the solution was cooled down to room temperature. Meanwhile, different amount of Silver Nitrate (16.99~33.97 mg, 0.1~0.2 mmol) was completely dissolved and ultra-sonicated in Oleyl amine (3 mLs) and Dichlorobenzene (1 mL). The AgNO3 solution was then injected into the flask and the final solution was kept at room temperature for 1 hour. At the end, the solution was diluted with ethanol to 50 mL and centrifuged at 8000 RPM for 10 minutes to precipitate out the copper nanoparticles from solution. The nanoparticles were then re-dispersed in 10 mL hexanes.

2.1.3. Cu Nanoparticles

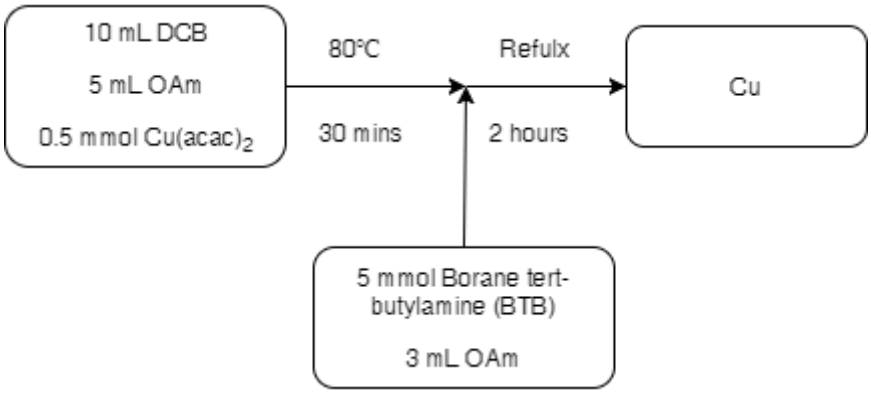

Figure 2-3 Schematic illustration of the synthetic route for Copper nanoparticles

Copper acetylacetonate (130 mg, 0.5 mmol), Dichlorobenzene (10 mLs) and Oleyl amine (5 mLs) was loaded into a glass three neck flask with a Schlenk line setup under constant stirring. The resulting mixture was heated to 80℃ while purging with Argon gas, at which the outlet was adjusted to a slight opening position to control the gas flowing at 1~2 bubbles per second. This solution was allowed to react for 30 minutes. At mean time, Borane tert-butylamine (BTB) (365.7 mg, 5 mmol) was dissolved and ultra-sonicated in Oleyl amine (5 mLs). Then the flask gas outlet was closed to prevent the solvent from evaporating off, and the BTB solution was injected, and the final solution was heated to reflux for 2 hours. A significant color change from clear/yellow to a deep red occurred after BTB injection. After cooling to room temperature, the solution was diluted with ethanol to 50 mL and centrifuged at 8000 RPM for 10 minutes to precipitate out the copper nanoparticles from solution. The nanoparticles were then re-dispersed in 10 mL hexanes.

2.1.4. Post-synthesis treatment

Carbon nanoparticles (15 mg) and Toluene (20 mLs) were added to a centrifuge tube. The Copper/Silver nanoparticles hexane solutions were added into the tube, and diluted with hexane to 50 mL and ultra-sonicated for at least 30 minutes to mix homogeneously. Then the solution was centrifuged at 10000 RPM for 5 minutes to precipitate out the Metal-Carbon nanoparticles mixture from solution. The nanoparticles were then re-dispersed and sonicated in 50 mL hexane, and centrifuged at 10000 RPM for 5 minutes. Repeated this procedure three times, and vacuumed dried overnight. At the end, the nanoparticles were weighed and collected for future tests.

2.2. Material characterization

Transmission electron microscopy (TEM) imaging was acquired on a 120 kV FEI Tecnai 12 TWIN microscope. Scanning transmission electron microscopy (STEM) and Elemental maps were performed on a Nion UltraSTEM200 with C3/C5 corrector in University of California Irvine. Inductively Coupled plasma mass spectrometry (ICP-MS) was performed on PerkinElmer NexION 300D with ICP. X-ray diffraction (XRD) patterns were collected on a Bruker D8 X-Ray Diffractometer equipped with a Cu Kα radiation source (λ=0.15406). X-ray photoelectron spectroscopy (XPS) characterization of individual nanoparticles were conducted on a Mg Kα X-ray source on a Perkin-Elmer photoelectron spectrometer. The X-ray source was operated at 15kV, 300W and a pass energy of 5.85eV was used to sample ejected photoelectrons from the Cu(2p) and Ag(3d) regions. Peak fitting of both regions was performed

using the XPSPEAK 4.1 software.

2.2.1. Transmission Electron Microscopy (TEM)

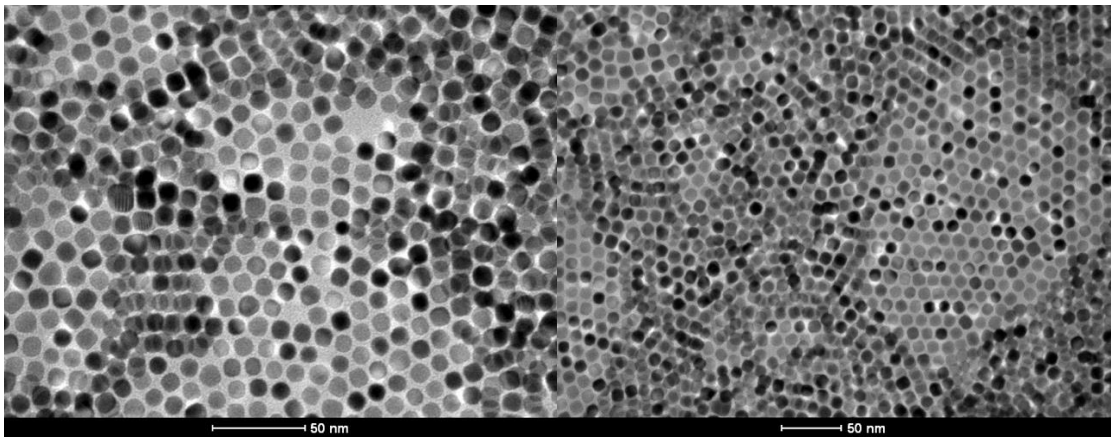

Figure 2-4 TEM images of s synthesized Silver nanoparticles

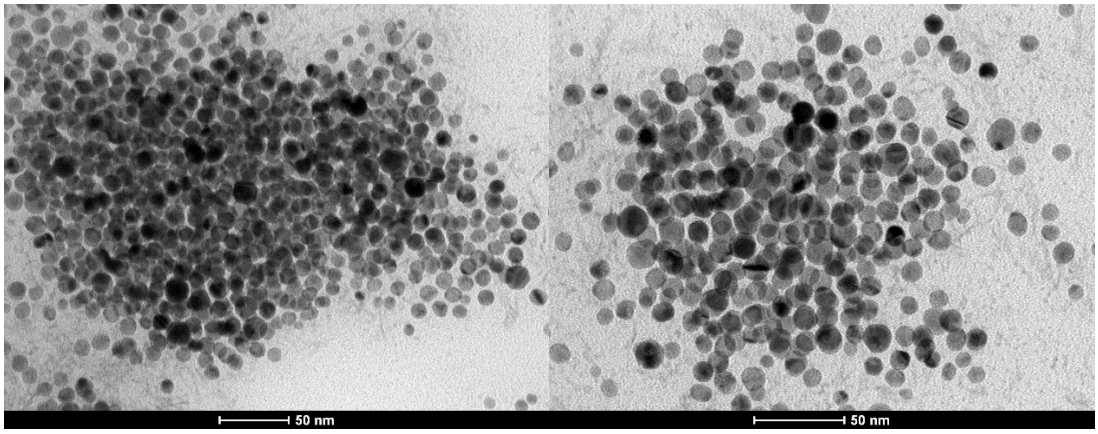

Figure 2-5 TEM images of as synthesized Cu@Ag1 nanoparticles with the low silver amount

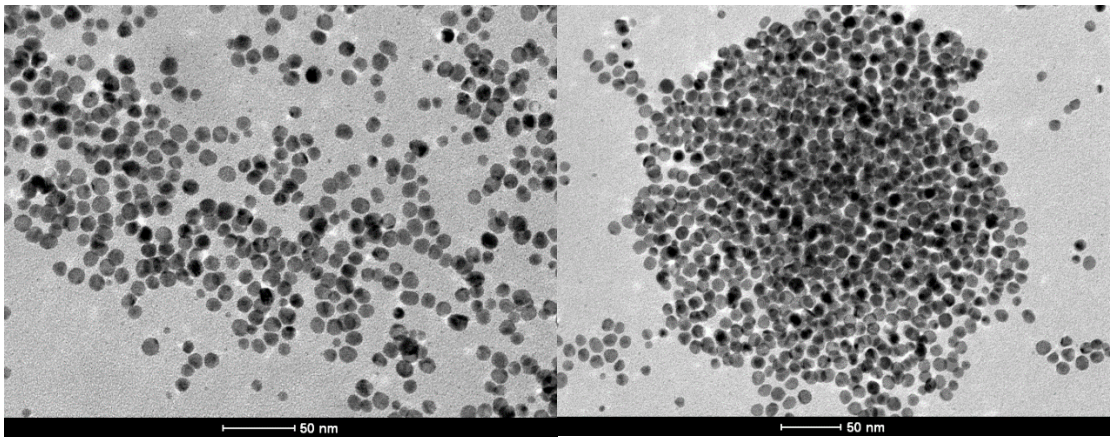

Figure 2-6 TEM images of as synthesized Cu@Ag2 nanoparticles with the high silver amount

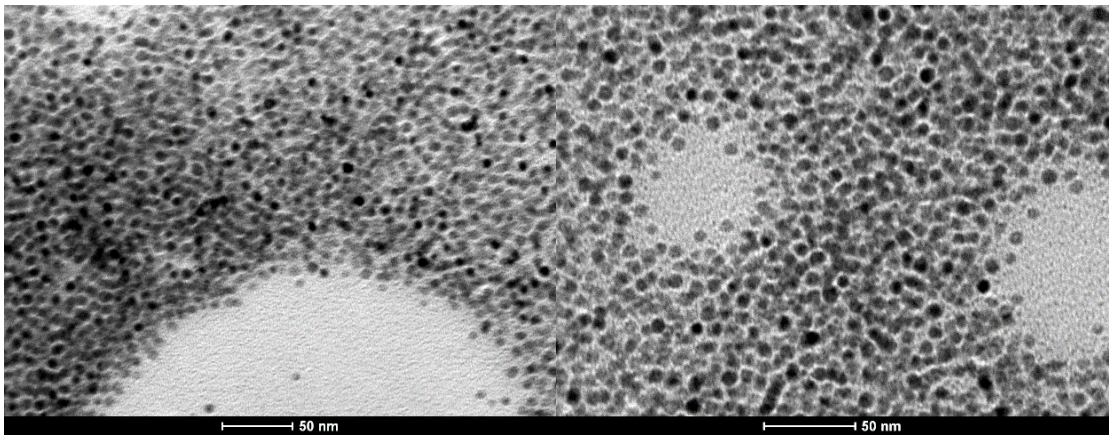

Figure 2-7 TEM images of as synthesized Cu nanoparticles

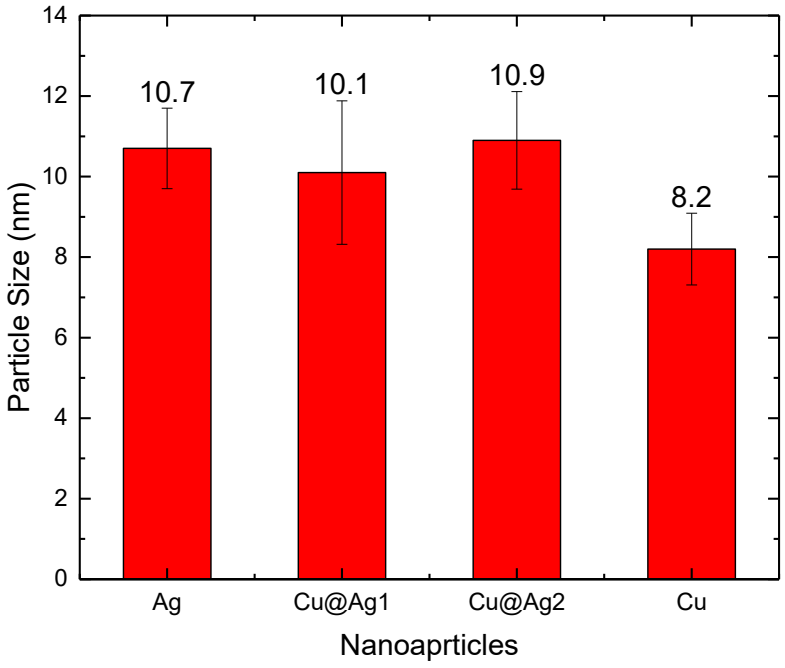

Figure 2-8 The summary of nanoparticles' sizes

The TEM images of silver nanoparticles, alloy core-shell nanoparticles, and copper nanoparticles are showed in Fig. 2-4 to 2-7. Also, we analyzed the sizes of these four nanoparticles. The average diameter of silver, Cu@Ag1, Cu@Ag2, and copper nanoparticles are 10.68 nm, 10.08 nm, 10.94 nm, and 8.21 nm (Fig. 2-8). The sizes were counted by NanoMeasurer software from Fudan University. Cu@Ag1 has lower silver amount, and the diameter is smaller than Cu@Ag2 nanoparticles. Because when the amount of silver increased, the silver shell becomes thicker.

2.2.2. Scanning transmission electron microscopy (STEM) and Elemental maps

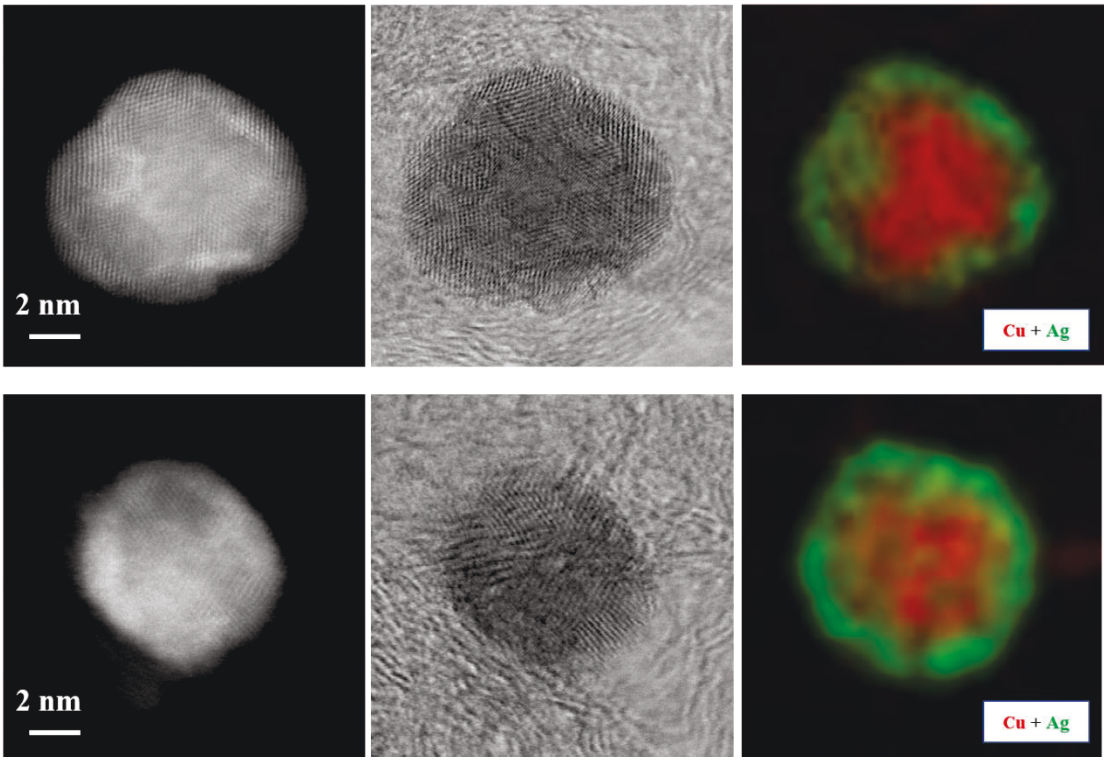

Figure 2-9 Representative STEM images and elemental maps collected for top Cu@Ag 1, and bottom Cu@Ag 2 nanoparticles.

The STEM images of core-shell nanoparticles are showing in Fig. 2-9. The dark field image clearly showed the core and shell materials have different contrast. In addition, the elemental maps gave us a very clear view of the nanoparticle elemental distribution. The silver atoms were accumulating at the shell, and copper atoms were only gathered at core area. Therefore, the STEM images intuitively verified our core-shell nanoparticles structure.

2.2.3. Inductively Coupled Plasma Mass Spectrometry (ICP-MS)

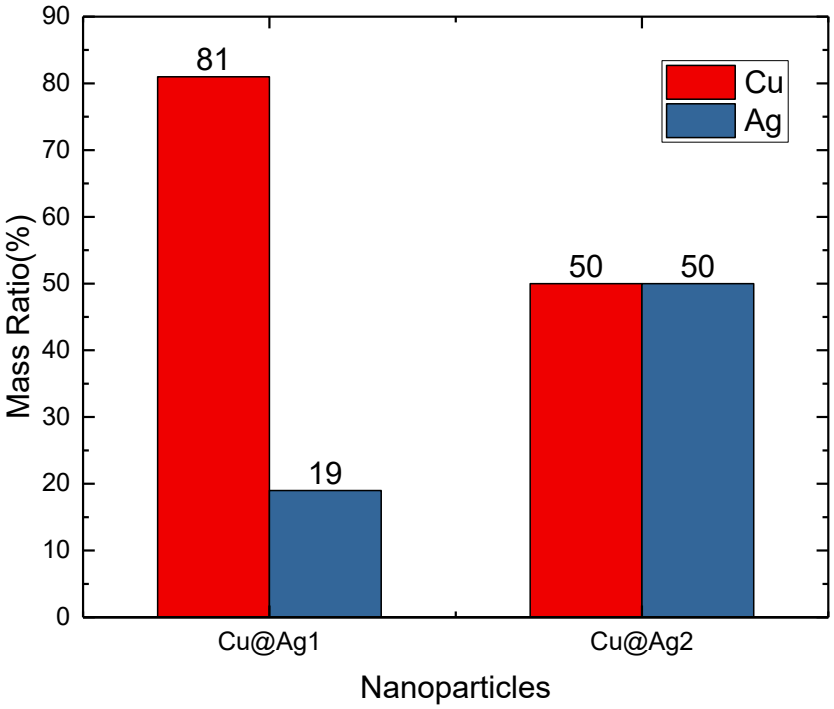

Figure 2-10 The result of ICP test showing the silver/copper mass ratio in each alloy nanoparticles

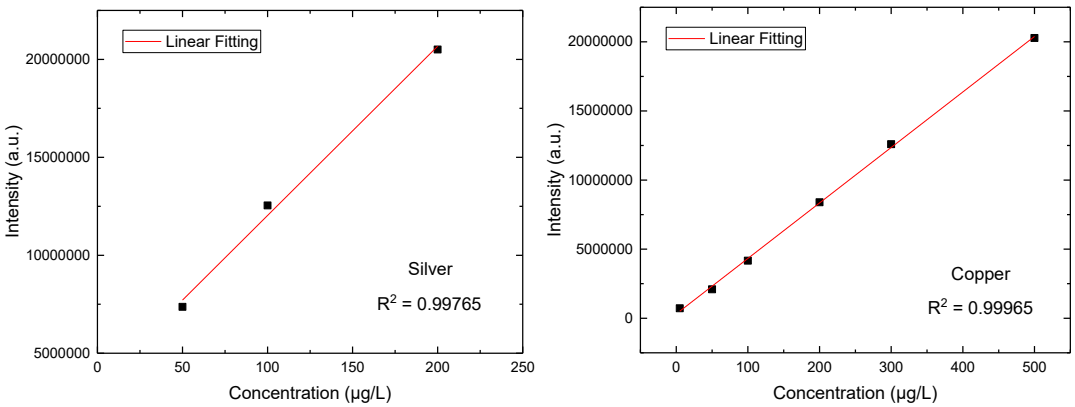

Figure 2-11 Calibration curves of Silver and Copper concentration used in ICP test

The ICP samples were immediately prepared after synthesis. 1 mg of each Silver and Copper nanoparticles were weighed out and dissolved in fresh made Aqua Regia overnight. The solutions were diluted 50 times and filtered by PTFE hydrophilic filter membrane. Before testing Nanoparticle samples, standard copper and silver calibration curves were obtained (Fig. 2-10). The two core-shell nanoparticles' Cu/Ag mass ratios were showed in Fig 2-9. In first nanoparticle, Copper occupied 81% mass, and the resting 19% is silver, and in the second nanoparticle, copper and silver have the same mass portion. Therefore, the ICP test results verified our successful control over silver/copper mass ratio.

2.2.4. X-ray Powder Diffraction (XRD)

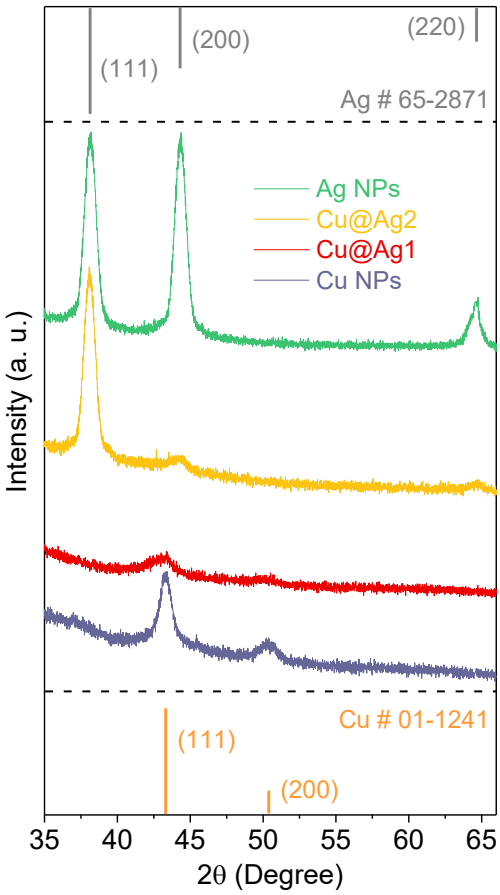

Figure 2-12 XRD patterns of the copper/silver nanoparticles. Peaks for Ag and Cu are marked at the top and the bottom for comparison. The experimental XRD patterns showing here are belong to silver nanoparticles, two silver/copper alloy nanoparticles, and copper nanoparticles from the top to bottom respectively.

Figure 2-12 shows the XRD patterns for the different materials. Standard Ag and Cu peaks are shown at the top and the bottom the diagram. The experimental XRD patterns of silver nanoparticles, two silver/copper alloy nanoparticles, and copper nanoparticles are shown from top to bottom respectively. It can be seen that, with the amount of silver decreasing, the silver pattern disappeared. The Cu@Ag1 nanoparticles have the lowest amount of silver. The XRD pattern is dominated by Cu, there is no significant Ag peak could be seen. The Cu@Ag2

nanoparticles have the most amount of silver, which have the strongest Ag (111) peak and inconspicuous Cu (200) peak. This result successfully verified the ratio of silver and copper metal content in each kind of nanoparticles. In addition, the XRD result reinforced the discovery from ICP test.

2.2.5. X-ray Photoelectron Spectroscopy (XPS)

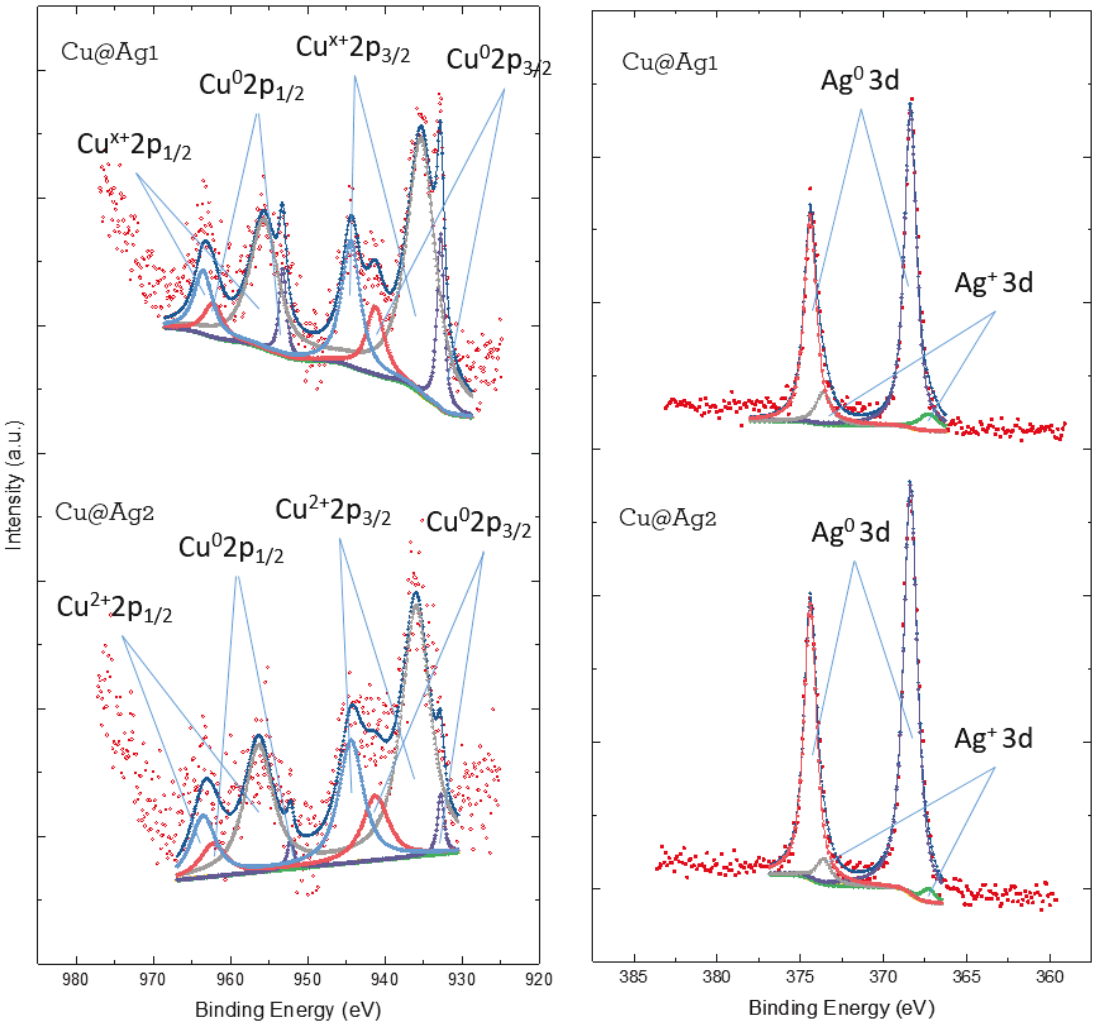

Figure 2-13 The XPS spectra results of Cu 2p (a) and Ag 3d (b) peak fit in the as-prepared Cu/Ag alloy nanoparticles. Cu@Ag1, Cu@Ag2 from top to bottom respectively.

Table 2-1 Cu^{x+}/Cu^0 ratios in two Cu@Ag alloy nanoparticles

Area	Cu@Ag1	Cu@Ag2
$Cu^0 2p$	3305.957	682.2751
$Cu^{2+} 2p$	28930.71	21110.41

Table 2-2 Ag^+/Ag^0 ratios in two Cu@Ag alloy nanoparticles

Area	Cu@Ag1	Cu@Ag2
$Ag^0 3d$	562.6389	420.6491
$Ag^+ 3d$	4658.817	6541.061

The surface composition of the Cu@Ag alloy nanoparticles was analyzed by the XPS, the spectrums of Cu 2p and Ag 3d (see Fig. 2-13). The XPS spectrum was corrected to the adventitious contaminated C 1s peak at 284.5 eV. In Fig. 2-13 a, the two peaks located at 932.00 eV and 951.20 eV are attributed to Cu^0 2p, and the rest eight peaks at 932.80 eV, 935.33 eV, 941.24 eV, 944.40 eV, 953.24 eV, 955.68 eV, 962.24 eV, and 963.53 eV correspond to Cu^{x+} 2p [36]. On the other hand, in Fig. 2-13 b, the two peaks located at 367.9 eV and 373.9 eV are assigned to Ag^+ 3d, and those at 368.6 and 374.6 eV are ascribed to the metal Ag^0 3d [37]. The Cu^0 2p peaks and the Ag^0 3d peaks indicated the elemental copper and silver at the base and surface of alloy nanoparticle. And the Cu-Ag alloyed particles are represented by Cu^{x+} 2p peaks and Ag^+ 3d peaks. Therefore, the molar ratio between area ratio between Ag^0 3d and Ag^+ 3d could be calculated from their area, which represent the ratio between the amount of silver atoms connected with silver atoms or copper atoms. The ratios results are showed in table 2-1 and table 2-2, and the Cu@Ag1 showed the lower Ag^0 amount, which is consistent with the

ICP-MS result. Therefore, the XPS results proved the silver element amount in each kinds of alloy nanoparticles again.

2.3. Catalyst preparation

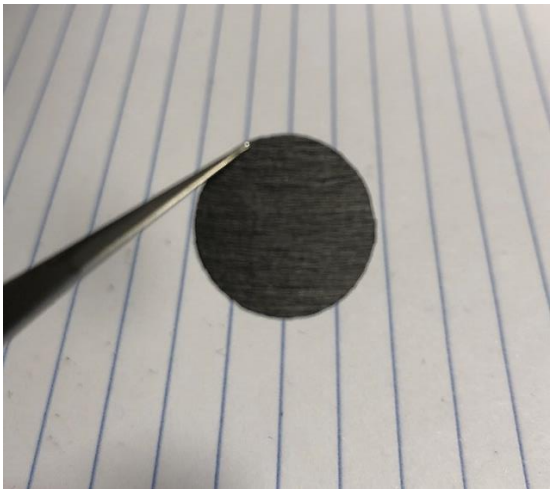

Figure 2-14 16 mm diameter Carbon fiber paper used as catalysts carrier

Figure 2-15 Air spray gun used for nanoparticle coating on carbon fiber paper

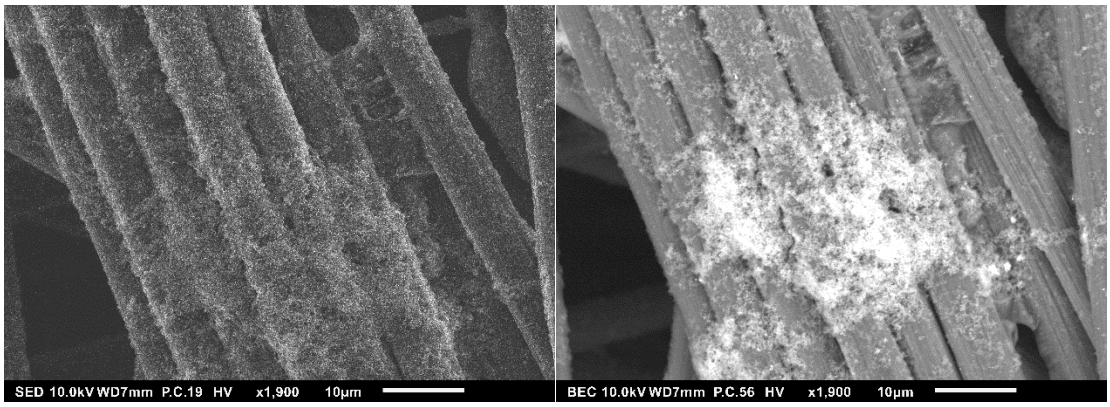

Figure 2-16 a) SEM image of Cu/Ag alloy nanoparticles with TANAKA carbon loaded on carbon fiber. b) SEM-BEC image of Cu/Ag alloy nanoparticles location on carbon fiber.

Toray Carbon paper (Full Cell Earth) was punched to 16 mm diameter small disks (Fig. 2-15), and immobilized on hotplate to evacuate all the moisture. 1 mg of each Silver and Copper nanoparticles were weighed out and diluted by isopropyl alcohol (IPA) (1 mL). The solutions were ultra-sonicated at least 30 minutes to ensure all the nanoparticles were disperse homogeneously. Then, air spray gun (Fig. 2-16) was used to load nanoparticles on the dried carbon fiber paper. Each side of the carbon paper was doped by 200 μLs solution, which equals to 200 μg of nanoparticles. Finally, the carbon paper was dried on a hotplate and collected to be used in the electrochemical experiments. The sprayed nanoparticles on carbon fibers are showed in Fig. 2-17.

2.4. Electrochemical Measurements

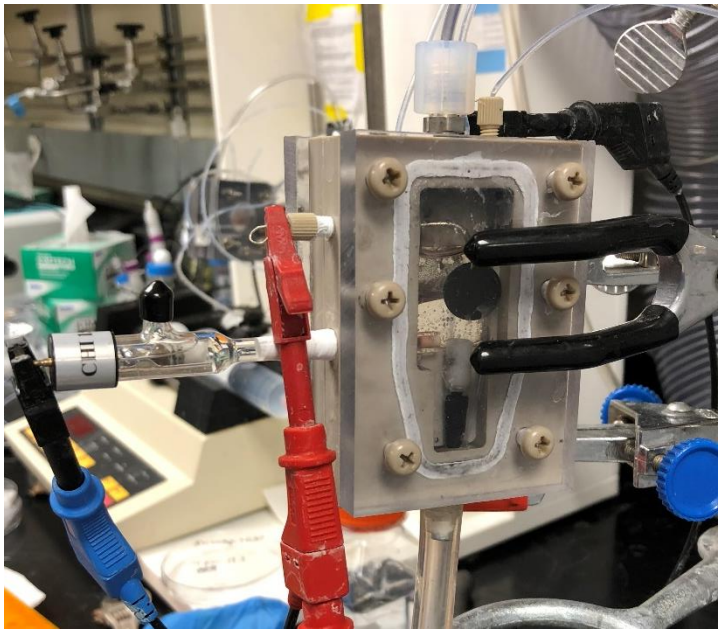

Figure 2-17 Electrochemical catalytical cell setup

The electro-catalytic activities of different nanoparticles were measured by a same protocol. We used a custom-made gas-tight electrolysis cell, and the AutoLab 302 potentiostat (Metrohm) electrochemistry testing station. Three-electrodes system (Fig. 2-18) was employed for our electrochemical measurements. A $Hg/HgSO_4$ reference electrode (Koslow Scientific), and a Platinum mesh (VWR) were used as counter electrode. The working electrode was a silver wire connecting to carbon paper doped with nanoparticles. The 0.1 M $KHCO_3$ solution was used as the electrolyte, and when the solution is CO_2 saturated, the pH was measured to be around 6.8. The CO_2 supply was controlled by a mass flow controller at a constant rate of 20 sccm. In addition, the working electrode and counter electrode were separated by an anion exchange membrane (Selemion Inc.).

At the beginning of the experiment, the carbon fiber paper was punched a small hole, and

hanged on the silver wire. Both cathode and anode compartments were immersed by electrolyte, and purged 20 sccm Helium gas for 30 minutes. At meantime, the external copper oxide at the nanoparticles were electrochemically reduced to copper by applying a voltage of -0.4 V vs. RHE. The reduction current was recorded by Autolab. Once the reduction current reached a relative steady state value, full reduction to copper surface had been achieved. Helium gas supply was shut down, and CO_2 (20 sccm) gas flow was switched on. All the materials were tested at voltage -0.4 V to -1 V vs. RHE, and each point had the duration of 30 minutes. The gas products were directly collected and analyzed by Gas chromatography – mass spectrometry (GCMS) (Shimadzu). Also, the electrolytes used in the CO_2 reduction test were collected to complete the Nuclear Magnetic Resonance (NMR) test to qualitatively and quantitatively analyze the liquid products. After the electrochemical test finished, all the used doped carbon papers were collected and dissolved by fresh made Aqua Regia, which would be analyzed by ICP test to verify the metal mass.

3 Discussion and results

3.1. Gas product analysis

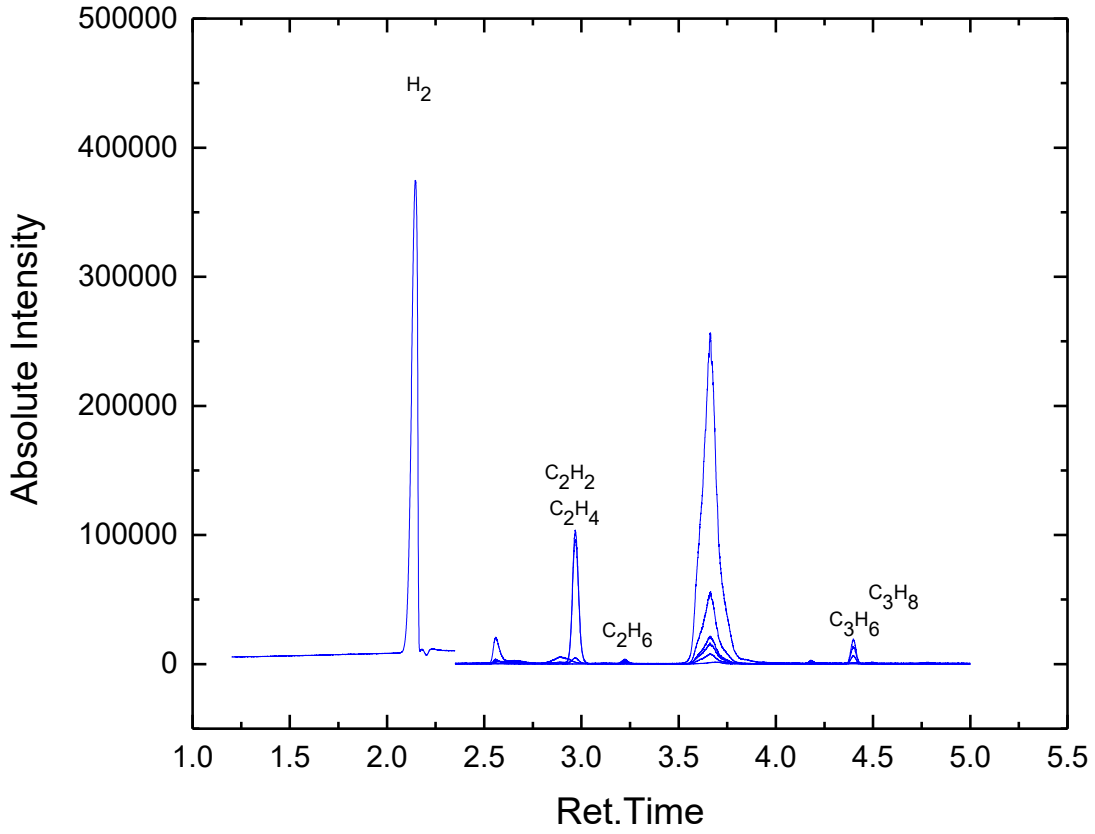

Figure 3-1 Representative GC-MS spectrum collected for the gas products from CO2 reduction by using Cu@Ag alloy core-shell nanoparticles.

The gas products of the electrochemical reduction of CO_2 were analyzed by using a GC-MS QP2010SE (Shimadzu) equipped with a Plot-Q column (Restek). Helium gas was used as the carrier gas. During the CO_2 reduction experiment, the gas samples were periodically taken every 6 minutes. So, each potential had 5 total measurements. The representative GC-MS measurement spectrum was showed in Fig. 3-1. The peak at 2.1 is attributed to hydrogen (H_2);

The peak at 3.0 is corresponded to acetylene (C_2H_2) and ethylene (C_2H_4); The peak located at 3.2 is assigned to ethane (C_2H_6); Also, the peak at 4.4 is ascribed as propane (C_3H_8) and propylene (C_3H_6). The averages of the

concentration of each gas product was reported in Table 3.1. The faradaic efficiencies of the gas products were calculated by using the following formula:

$$\mathrm{FE\%} = \frac{\mathrm{ppm} \times \mathrm{flow\ rate} \times \frac{\mathrm{nFP}}{\mathrm{RT}}}{\mathrm{J}} \times 100\%$$

Where the ppm is the gas products concentrations obtained from GC-MS, n is the number of electrons transferred in each CO_2 reduction reaction, F is the faraday constant. J is the partial current densities, which could be calculated by using the following formula:

$$\mathrm{J} = \frac{\mathrm{ppm} \times \mathrm{flow\ rate} \times \frac{\mathrm{nFP}}{\mathrm{RT}}}{\mathrm{geometric\ surface\ area}}$$

Table 3-1 Summary of faradaic efficiencies of Hydrogen, Carbon Monoxide, and Ethylene at various potentials on four different nanoparticles

	Faradaic Efficiency (FE%)								
E	**Ag**		**Cu@Ag1**		**Cu@Ag2**		**Cu**		
V vs. RHE	H_2	CO	H_2	CO	H_2	CO	H_2	CO	C_2H_4
-0.5	92.30	8.34	89.29	10.50	86.29	13.99	79.84	11.69	0.30
-0.6	89.82	10.12	84.62	15.75	68.58	22.97	76.84	17.34	0.35
-0.7	83.65	15.62	64.80	21.65	63.82	32.29	73.01	20.21	1.31
-0.8	75.07	25.43	52.35	37.75	54.88	43.09	70.19	21.16	4.48
-0.9	59.76	39.87	36.55	55.18	42.56	54.11	68.36	20.05	7.01
-1	46.90	50.39	29.03	65.95	41.92	56.77	65.13	19.37	10.74

3.2. Liquid product analysis

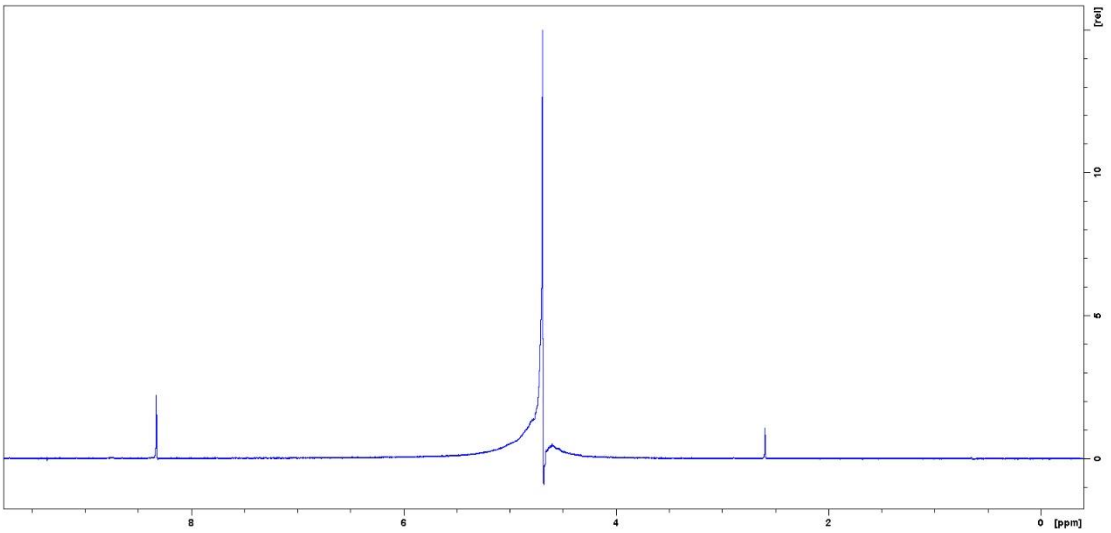

Figure 3-2 Sample NMR spectrum collected for the liquid products from CO2 reduction by using Cu@Ag alloy core-shell nanoparticles.

Liquid products were analyzed by using 400 MHz NMR spectrometer (Bruker) with D2O solvent and Dimethyl sulfoxide (DMSO) as internal standard. After 30 minutes of electroreduction reaction, 665 μL of electrolyte containing CO2 reduction liquid products was mixed with 70 μL of 5 mM DMSO in D2O. Fig. 3-2 is a sample NMR spectrum,

and Fig. 3-2 is the corresponding faradaic efficiency data. The peak at 2.62 ppm is attributed to DMSO standard. The peak at 4.8 ppm is corresponded to D2O solvent. The peak located at 8.4 ppm is assigned to formic acid. The NMR peaks area were integrated to determine the concentration of formic acid in electrolyte. The averages of the concentration of each liquid product were reported in Table 3.2. The faradaic efficiencies of the liquid products were calculated by using the following formula:

$$\mathrm{FE\%} = \frac{nMVF}{0.95\mathrm{tJ}} \times 100\%$$

Where n is the number of electrons transferred in each CO_2 reduction reaction, M is the concentration of the liquid product in the NMR sample, V is the liquid volume in the electro-catalytic cell, F is the faraday constant, 0.95 is the dilution rate in making NMR sample, t is the time of electro-reduction, and J is the average current densities.

Table 3-2 Summary of faradaic efficiencies of Formic Acid at various potentials on four different nanoparticles.

E	**Formic Acid Faradaic Efficiency (FE%)**			
V vs. RHE	**Ag**	**Cu@Ag1**	**Cu@Ag2**	**Cu**
-0.5	-	-	-	8.342
-0.6	-	-	7.773	6.112
-0.7	-	13.289	7.108	5.914
-0.8	-	9.627	5.424	4.585
-0.9	-	7.924	3.149	4.874
-1.0	2.586	5.453	1.599	4.547

3.3. Comparison

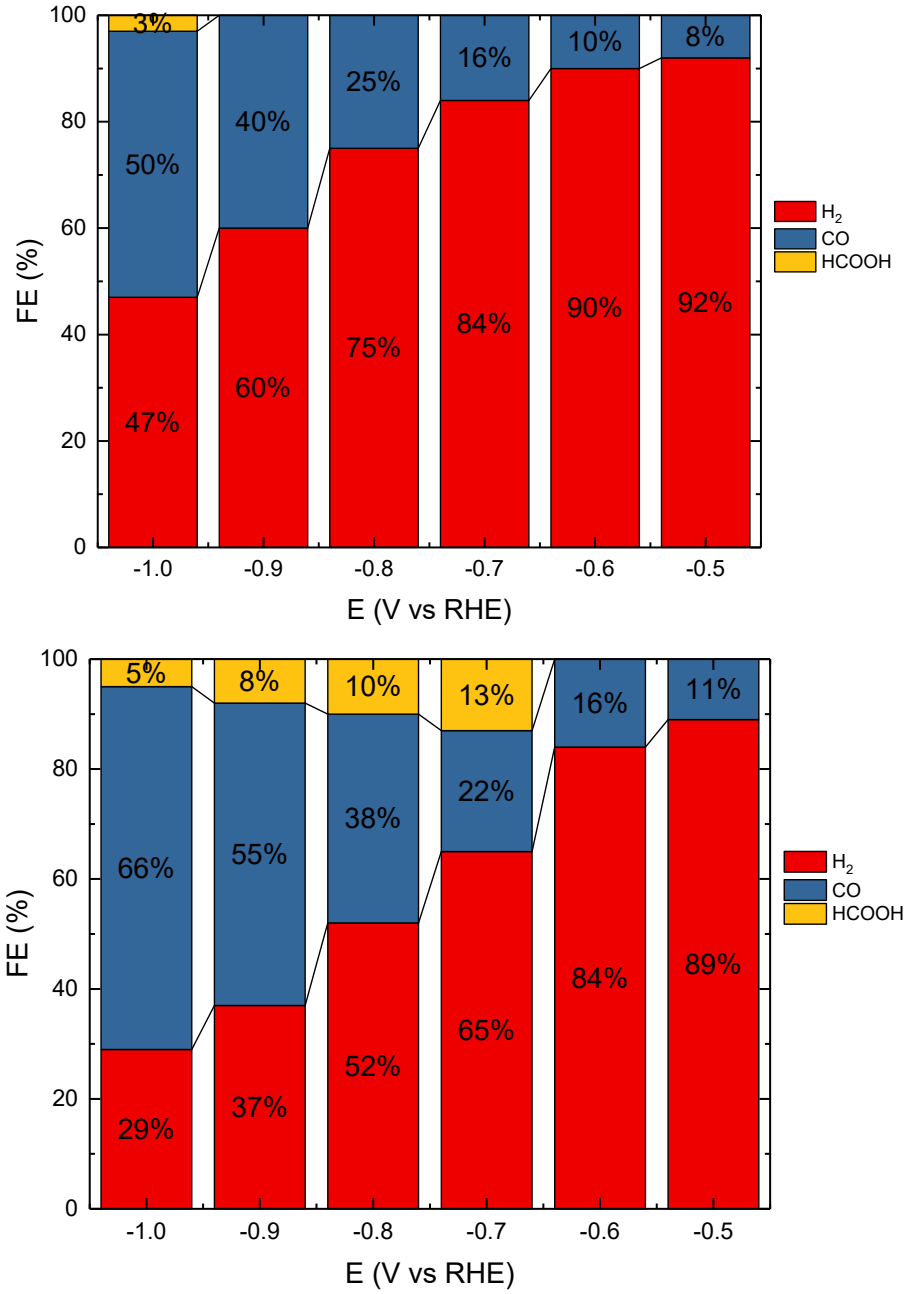

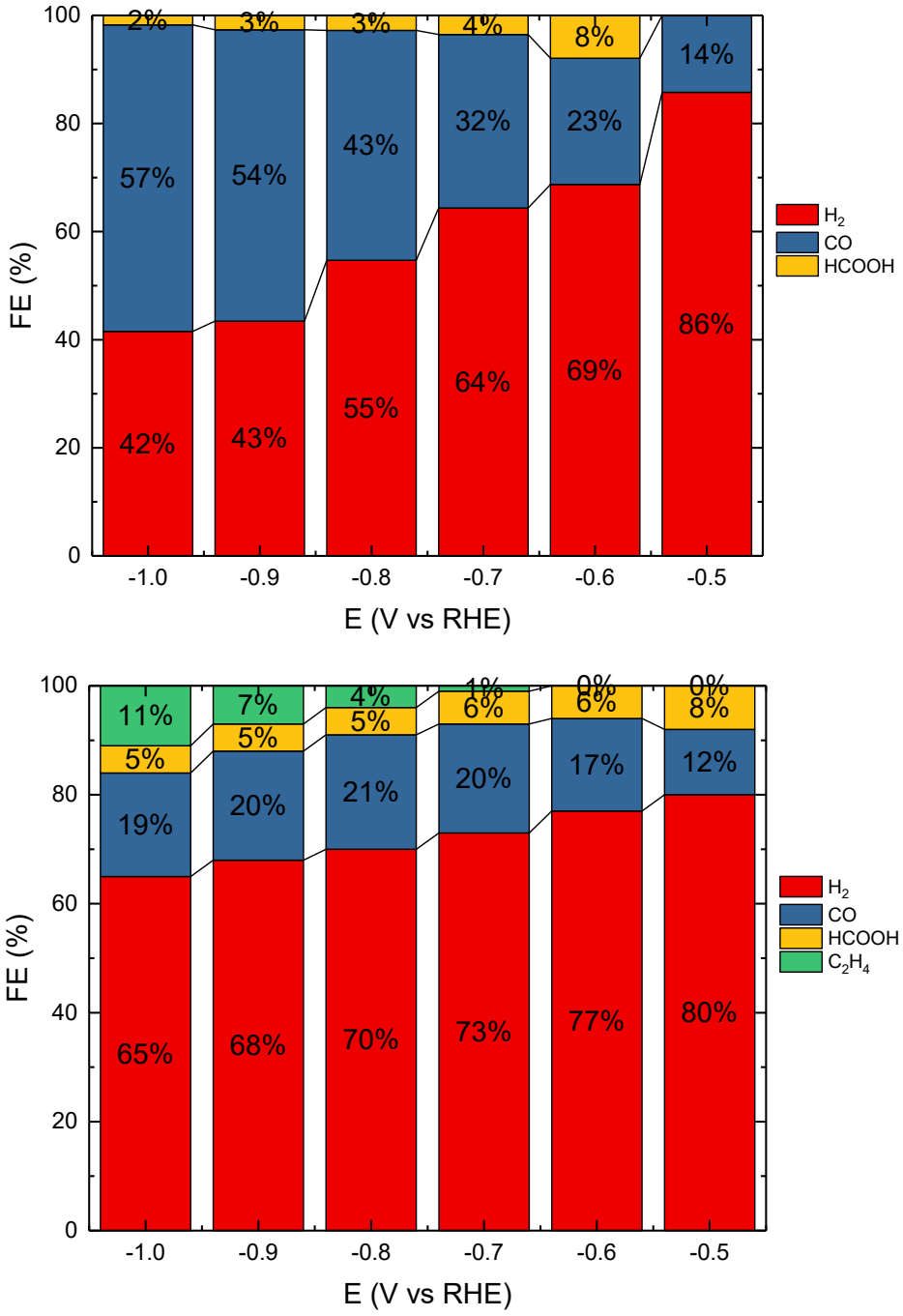

Figure 3-3 Faradaic efficiencies for the production of hydrogen, carbon monoxide, and formic acid for Ag, Cu@Ag1, Cu@Ag2, and Cu nanoparticles

Through the studies, hydrogen, carbon monoxide, and formic acid were found to be the major products of CO2 reduction. Only Copper nanoparticle showed ethylene product. Several

potentials from -500 mV to -1000 mV were selected to reduce the CO2 on Ag, Cu@Ag, and Cu nanoparticles catalysts for 30 minutes. Faradaic efficiency (FE) for H2, CO, HCOOH and C_2H_4 were calculated by using the current density and produced product concentration as shown in Fig. 3-3. In the case of the Ag nanoparticle catalyst (Fig. 3-3 a), the FE was dominated by Hydrogen evolution reaction (>75%) at low over-potentials (>-0.8 V). FE of HER decreased to 47% at -1 V, and only 2.59% of formic acid presented. For the Cu@Ag1 alloy core-shell nanoparticle catalyst (Fig. 3-3 b), which has the lowest silver metal amount, showed only 29% of HER Faradaic efficiency at -1 V. At mean time, the selectivity of CO increased to 65%. Formic acid firstly present at -0.7 V with 13% FE, and decreased to 5% FE at -1 V. The FE data of Cu@Ag2 alloy core-shell nanoparticle catalyst were showed in Fig. 3-3 c. At a lowly negative potential form -0.5 V to -0.8 V, the FE of Hydrogen decreased from 86% to 54%. However, at a highly negative potential from -0.7 V to -1 V, the FE of CO increased from 32% to 56%, and the selectivity of formic acid present from 8% to 1.6%. In addition, the performance of Cu nanoparticle catalysts was showed in Fig. 3-3 d. In the range of -0.5V to -1V, the FE of HER decreased from 80% to 65%. The FE of CO was fluctuated 12% to 21%. Also, the selectivity of HCOOH decreased from 8% to 5% at the range from -0.5V to -1V. Ethylene was unique in Cu Nanoparticles, and the faradaic efficiency increased from 1% to 11% at -0.7V to -1V.

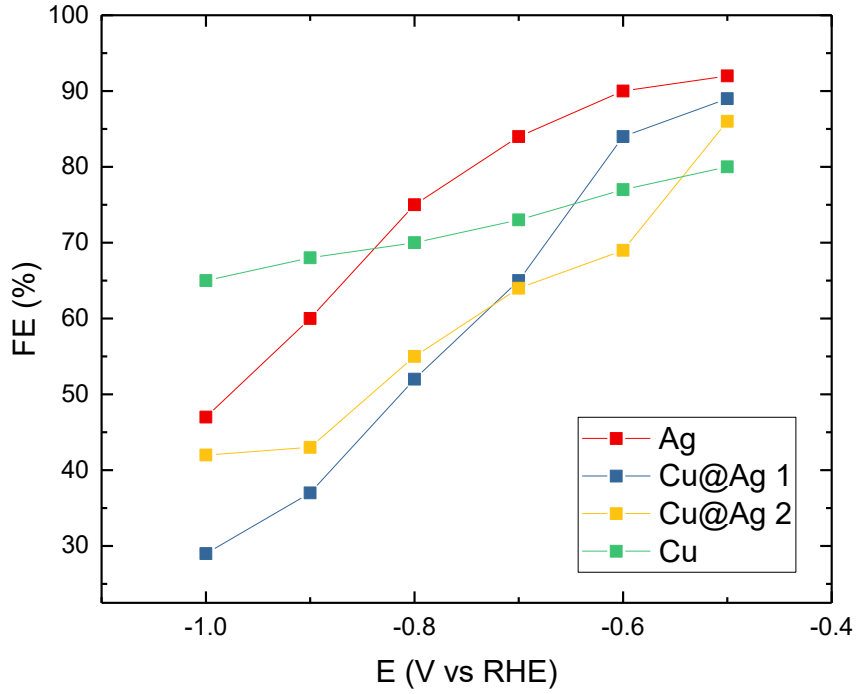

Figure 3-4 Faradaic efficiencies for hydrogen evolution reaction

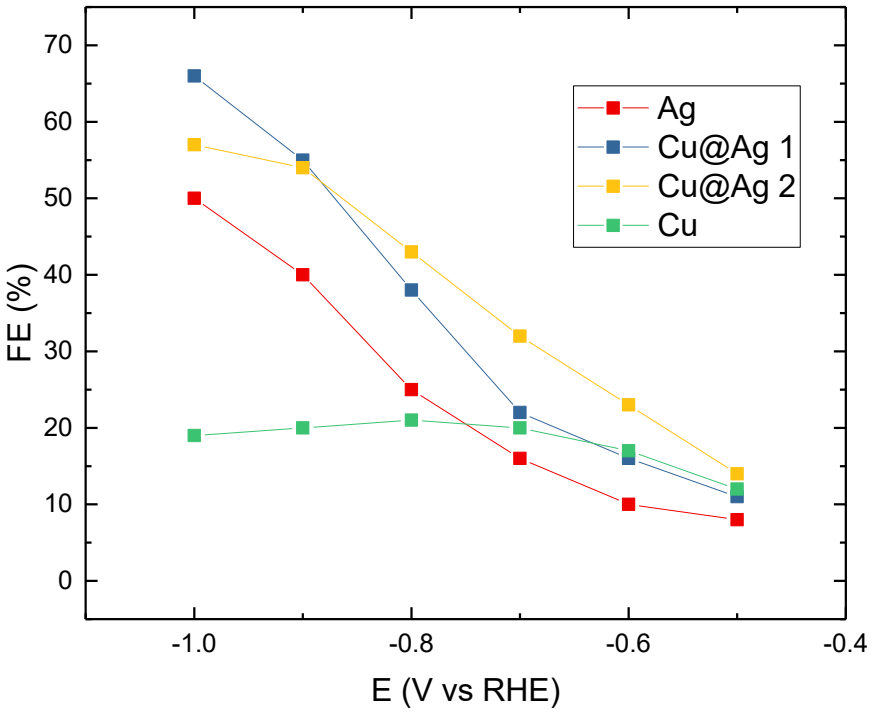

Figure 3-5 Faradaic efficiencies for Carbon Monoxide generation

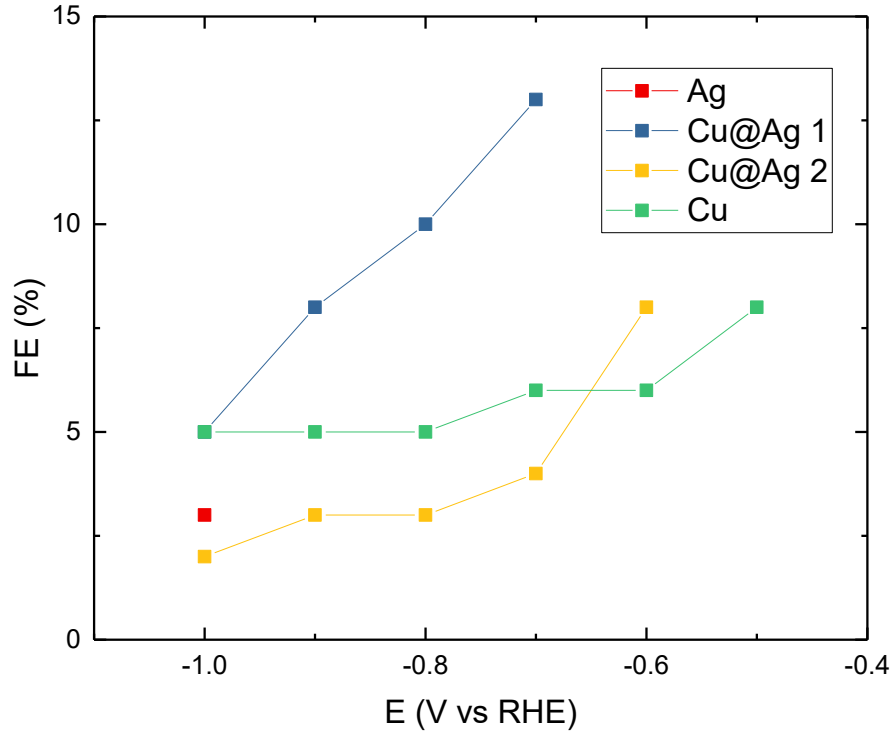

Figure 3-6 Faradaic efficiencies for Formic acid generation

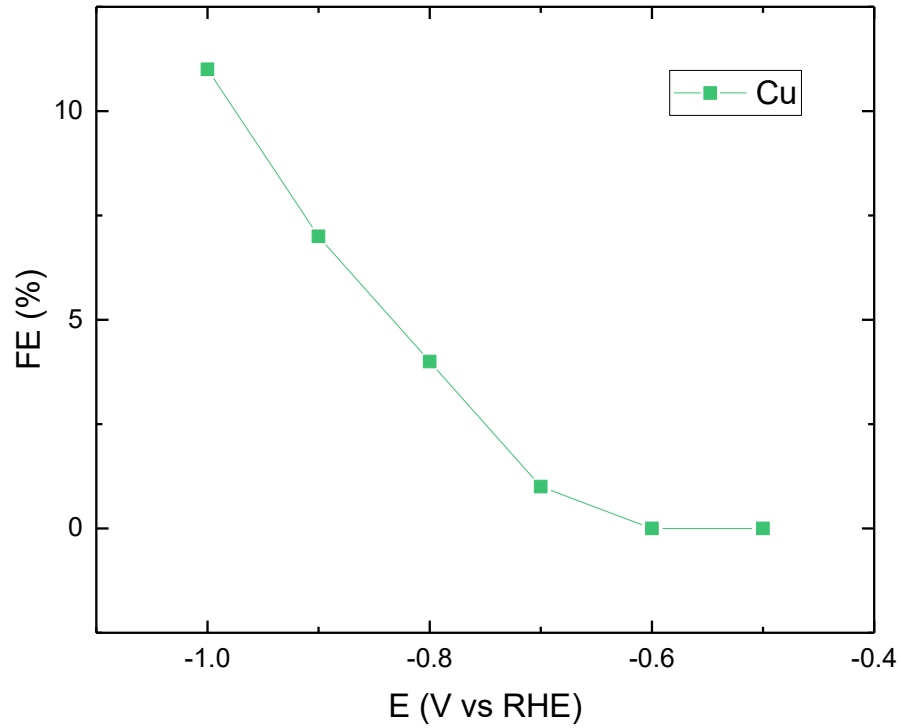

Figure 3-7 Faradaic efficiencies for Ethylene generation

To better illustrate the differences in catalytic performance. We have compared the faradic

efficiency of each specific product of the four nanoparticles catalysts. (Fig. 3-4 to 3-7) For the HER selectivity, Silver nanoparticles showed the highest FE at low over-potential range (-0.4V ~ -0.8V), however, the faradaic efficiency decreased rapidly at -0.9V to -1V. Therefore, Copper nanoparticles showed the worst restrain ability in this range. Cu@Ag alloy nanoparticles showed very promising HER restrain selectivity. In addition, the surface containing the lowest silver amount had the lowest HER FE. The synergistic effect of copper and silver atoms successfully suppress the hydrogen evolution. The FE of CO is summarized in Fig. 3-5. Cu@Ag2 was showing the highest selectivity, and Cu@Ag1 exceeded Cu@Ag2 nanoparticle's selectivity at -1V. Copper showed significantly lower selectivity of CO at -0.8V to -1V range. The selectivity of HCOOH were concluded in the Fig. 3-6. Cu@Ag1 nanoparticles showed strong favor of formic acid. Cu@Ag2 and copper nanoparticles showed lower and similar performances. However, only at -1V formic acid presented in silver catalytic products, and the selectivity was also very low. In conclusion, Cu@Ag1 nanoparticles showed the highest overall CO2 conversion selectivity, and the lowest HER selectivity. In addition, among all the catalysts, it showed the highest faradic efficiency of formic acid, which has the highest economic value in all the possible products. Therefore, both core-shell nanoparticles improved the performance of CO_2 electrochemical reduction, and increased the selectivity of valuable products.

4 Conclusions and Future Steps

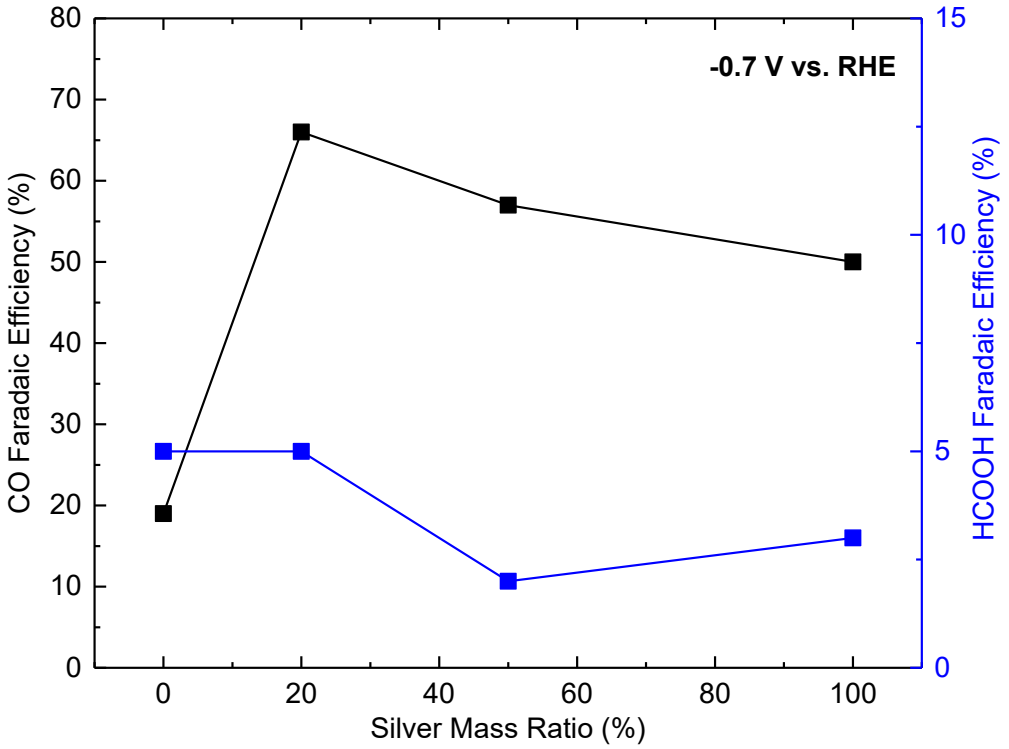

Figure 4-1 Faradaic efficiencies of Carbon Monoxide and Formic acid of four nanoparticles at -1 V vs. RHE.

Our study presents a one-pot wet chemical synthesis method of core-shell nanoparticles with silver/copper alloy surface. Our extensive characterizations provide robust support for our claims of structural and exterior properties with experimental measurement results. With our finding, we provide a summary analysis on the correlations between the structural information and catalytic activity. Fig. 4-1 shows the performance of four nanoparticles at -1V vs. RHE. The copper silver core-shell nanoparticle with a thinner silver shell has higher and more unitary selectivity on carbon monoxide. Our work has advanced the understanding of Ag/Cu based nanoscale catalytic materials, which could be valuable for the further development of the next generation of electro-catalytic materials for CO_2 reduction.

5 References

1 Ghosh Chaudhuri, R. & Paria, S. Core/shell nanoparticles: classes, properties, synthesis mechanisms, characterization, and applications. *Chem Rev* **112**, 2373-2433, doi:10.1021/cr100449n (2012).

2 Peng, Y.-h. *et al.* Study on synthesis of ultrafine Cu–Ag core–shell powders with high electrical conductivity. *Appl Surf Sci* **263**, 38-44, doi:10.1016/j.apsusc.2012.08.066 (2012).

3 Wang, L. *et al.* Core–Shell Nanostructured Cobalt–Platinum Electrocatalysts with Enhanced Durability. *Acs Catal* **8**, 35-42, doi:10.1021/acscatal.7b02501 (2017).

4 Wang, L. *et al.* Plating Precious Metals on Nonprecious Metal Nanoparticles for Sustainable Electrocatalysts. *Nano Lett* **17**, 3391-3395, doi:10.1021/acs.nanolett.7b00046 (2017).

5 Zhao, J., Zhang, D. & Zhao, J. Fabrication of Cu–Ag core–shell bimetallic superfine powders by eco-friendly reagents and structures characterization. *J Solid State Chem* **184**, 2339-2344, doi:10.1016/j.jssc.2011.06.032 (2011).

6 Peng, Z. M. & Yang, H. Designer platinum nanoparticles: Control of shape, composition in alloy, nanostructure and electrocatalytic property. *Nano Today* **4**, 143-164 (2009).

7 Au, L. *et al.* Synthesis and Optical Properties of Cubic Gold Nanoframes. *Nano Res* **1**, 441-449, doi:10.1007/s12274-008-8046-z (2008).

8 da Silva, A. G. M., Rodrigues, T. S., Haigh, S. J. & Camargo, P. H. C. Galvanic replacement reaction: recent developments for engineering metal nanostructures towards catalytic applications. *Chem Commun (Camb)* **53**, 7135-7148, doi:10.1039/c7cc02352a (2017).

9 Clark, E. L., Hahn, C., Jaramillo, T. F. & Bell, A. T. Electrochemical CO2 Reduction over Compressively Strained CuAg Surface Alloys with Enhanced Multi-Carbon Oxygenate Selectivity. *J Am Chem Soc* **139**, 15848-15857, doi:10.1021/jacs.7b08607 (2017).

10 Jones, J.-P., Prakash, G. K. S. & Olah, G. A. Electrochemical CO2Reduction: Recent Advances and Current Trends. *Isr J Chem* **54**, 1451-1466, doi:10.1002/ijch.201400081 (2014).

11 Lim, H. K. & Kim, H. The Mechanism of Room-Temperature Ionic-Liquid-Based Electrochemical CO(2) Reduction: A Review. *Molecules* **22**, doi:10.3390/molecules22040536 (2017).

12 Singh, A. K. & Xu, Q. Synergistic Catalysis over Bimetallic Alloy Nanoparticles. *Chemcatchem* **5**, 652-676, doi:10.1002/cctc.201200591 (2013).

13 Jiang, H. L. & Xu, Q. Recent progress in synergistic catalysis over heterometallic nanoparticles. *J Mater Chem* **21**, 13705-13725, doi:10.1039/c1jm12020d (2011).

14 Hermannsdorfer, J. *et al.* Ni/Pd@MIL-101: synergistic catalysis with cavity-conform Ni/Pd nanoparticles. *Angew Chem Int Ed Engl* **51**, 11473-11477, doi:10.1002/anie.201205078 (2012).

15 Jiang, H. L., Akita, T., Ishida, T., Haruta, M. & Xu, Q. Synergistic catalysis of Au@Ag core-shell nanoparticles stabilized on metal-organic framework. *J Am Chem Soc* **133**, 1304-1306, doi:10.1021/ja1099006 (2011).

16 Kim, D., Resasco, J., Yu, Y., Asiri, A. M. & Yang, P. Synergistic geometric and electronic effects for electrochemical reduction of carbon dioxide using gold-copper bimetallic nanoparticles. *Nat Commun* **5**, 4948, doi:10.1038/ncomms5948 (2014).

17 Society, A. M. (eds Jessica Blunden & Derek S. Arndt) (2017).

18 Sanctuaries, N. M. (ed National Oceanic and Atmospheric Administration) (Climate Interpreter, 2016).

19 Administration, U. S. E. I. *Americans use many types of energy*, <https://www.eia.gov/energyexplained/?page=us_energy_home> (2017).

20 Administration, U. S. E. I. *Monthly Energy Review*, <https://www.eia.gov/totalenergy/data/monthly/> (2017).

21 Lindsey, R. *Climate Change: Atmospheric Carbon Dioxide*, <https://www.climate.gov/news-features/understanding-climate/climate-change-atmospheric-carbon-dioxide> (2017).

22 Laboratory, E. S. C. T. a. N. s. J. P. & Technology, C. I. o. *Carbon Dioxide*, <https://climate.nasa.gov/vital-signs/carbon-dioxide/> (2018).

23 Laboratory, E. S. C. T. a. N. s. J. P. & Technology, C. I. o. *Global Temperature*, <https://climate.nasa.gov/vital-signs/global-temperature/> (2018).

24 Laboratory, E. S. C. T. a. N. s. J. P. & Technology, C. I. o. *Arctic Sea Ice Minimum*,

<https://climate.nasa.gov/vital-signs/arctic-sea-ice/> (2018).

25 Laboratory, E. S. C. T. a. N. s. J. P. & Technology, C. I. o. *Ice Sheets*, <https://climate.nasa.gov/vital-signs/ice-sheets/> (2018).

26 Laboratory, E. S. C. T. a. N. s. J. P. & Technology, C. I. o. *Sea Level*, <https://climate.nasa.gov/vital-signs/sea-level/> (2018).

27 Gattrell, M., Gupta, N. & Co, A. A review of the aqueous electrochemical reduction of CO2 to hydrocarbons at copper. *J Electroanal Chem* **594**, 1-19, doi:10.1016/j.jelechem.2006.05.013 (2006).

28 Chen, Y. H., Li, C. W. & Kanan, M. W. Aqueous CO2 Reduction at Very Low Overpotential on Oxide-Derived Au Nanoparticles. *J Am Chem Soc* **134**, 19969-19972, doi:10.1021/ja309317u (2012).

29 Hoshi, N., Kato, M. & Hori, Y. Electrochemical reduction of CO2 on single crystal electrodes of silver Ag(111), Ag(100) and Ag(110). *J Electroanal Chem* **440**, 283-286, doi:Doi 10.1016/S0022-0728(97)00447-6 (1997).

30 Min, X. Q. & Kanan, M. W. Pd-Catalyzed Electrohydrogenation of Carbon Dioxide to Formate: High Mass Activity at Low Overpotential and Identification of the Deactivation Pathway. *J Am Chem Soc* **137**, 4701-4708, doi:10.1021/ja511890h (2015).

31 Kuhl, K. P., Cave, E. R., Abram, D. N. & Jaramillo, T. F. New insights into the electrochemical reduction of carbon dioxide on metallic copper surfaces. *Energ Environ Sci* **5**, 7050-7059, doi:10.1039/c2ee21234j (2012).

32 Hori, Y., Kikuchi, K. & Suzuki, S. Production of Co and Ch4 in Electrochemical

Reduction of Co2 at Metal-Electrodes in Aqueous Hydrogencarbonate Solution. *Chem Lett*, 1695-1698, doi:DOI 10.1246/cl.1985.1695 (1985).

33 Chernyshove, I. *CO2 to Fuels*, <http://blogs.cuit.columbia.edu/ic2228/co2-to-fuels/> (2015).

34 Takashima, T., Suzuki, T. & Irie, H. Electrochemical carbon dioxide reduction on copper-modified palladium nanoparticles synthesized by underpotential deposition. *Electrochim Acta* **229**, 415-421, doi:10.1016/j.electacta.2017.01.171 (2017).

35 Mancier, V., Rousse-Bertrand, C., Dille, J., Michel, J. & Fricoteaux, P. Sono and electrochemical synthesis and characterization of copper core-silver shell nanoparticles. *Ultrason Sonochem* **17**, 690-696, doi:10.1016/j.ultsonch.2009.12.009 (2010).

36 Li, S. *et al.* Synthesis of octahedral and cubic Cu2O microcrystals in sub- and super-critical methanol and their photocatalytic performance. *J Mater Sci* **50**, 4115-4121, doi:10.1007/s10853-015-8967-3 (2015).

37 Bao, Y. & Chen, K. AgCl/Ag/g-C3N4 Hybrid Composites: Preparation, Visible Light-Driven Photocatalytic Activity and Mechanism. *Nano-Micro Lett* **8**, 182-192, doi:10.1007/s40820-015-0076-y (2015).

Fei Xu

(C) 302-588-2503
(E) fxu9@jhu.edu
116 W. University Pkwy, APT 913
Baltimore, MD, 21218

Education

Baltimore, MD, USA
2016-2018

Johns-Hopkins University
Master's degree of Chemical and Biomolecular Engineering

Newark, DE, USA
2012-2016

University of Delaware
Bachelor's degree of Chemical and Biomolecular Engineering
Minor in Biochemical Engineering
Minor in Economics

Skills

- Matlab, Simulink, Aspen Plus®, AFT Fathom.
- ANSYS Fluent, Autodesk Inventor, OriginLab, Python and Microsoft Office.
- Nuclear magnetic resonance (NMR), Gas chromatography–mass spectrometry (GC/MS), X-ray Diffraction (XRD), Scanning electron microscope (SEM), Transmission electron microscope (TEM)

Experiences

Teaching Assistant
Baltimore, Maryland
September 2017-present

Johns-Hopkins University, Thermodynamics, Statistical Mechanics, and Kinetics (EN.540.630)
- Graded homework for 40 of students
- Answered questions from students

Master's thesis Research
Baltimore, Maryland
September 2016-present

Johns-Hopkins University, Dr. Chao Wang's Lab
- Lithium and Lithium alloy based electro-catalysis
- Lithium-Air batteries
- Gas phase electro-catalysis
- Nano-particles synthesis

Internship
Ningbo, Zhejiang, China
June – August 2016

Haode Chemical Co., Ltd.
- Initiated the distillation, isomerization of Butane, and MTBE manufacture and pyrolysis process
- Adjusted the distillation column to reach designed product purity
- Optimized the purge flow to save cost

Undergraduate Research
Newark, Delaware
2014-2016

University of Delaware, Dr. Yushan Yan's Lab
- All-Iron Redox Flow Battery
- Organic-Inorganic membraneless Redox Flow Battery
- Porous Copper Electrode

Teaching Assistant
Newark, Delaware
February – June 2015

University of Delaware, Applied Math for Chemical Engineering (MATH305)
- Graded course Matlab homework for 80 of students

Internship
Fuzhou, Fujian, China
June - August 2013

Fujian Southeast Electrochemical Co., Ltd.
- Initiated the manufacturing process of TDI and Sodium hydroxide
- Led the HSE regulation and management
- Found and remedied several potential safety hazards

Internship
Xiamen, Fujian, China
June - August 2012

Shanghai International Port Logistics (Xiamen) Co., Ltd.:
- Served for the logistics of ExxonMobil refinery plant products: polythene (PE) and polypropylene (PP).
- Optimized the truck fleets assignments, and increased the efficiency of truck loading.

Internship
Ningbo, Zhejiang, China
April - May 2012

Ningbo Zhuoyuan Economic and Trade Development (Group) Co., Ltd.
- Worked in Toluene, Xylene and Ethylene-vinyl acetate (EVA) marketing subsidiary.
- Communicated with suppliers and clients.

Publications

- Gong, K., Xu, F., et al. "An All-Soluble All-Iron Aqueous Redox-Flow Battery." ACS Energy Letters (2016).

- Gong, K., Xu., F., Lehrich, M.X., et al. "Exploiting Immiscible Aqueous-Nonaqueous Electrolyte Interface Towards a Membraneless Redox-Flow Battery Concept" journal of electrochemical society (2017).

Activities

Johns-Hopkins University
Baltimore, Maryland
September 2016-present

Volunteer
- STEM Achievement in Baltimore Elementary Schools (SABES).
- Tutored elementary school students to help them to engage STEM topics projects.

University of Delaware
Newark, Delaware
2012 – 2016

Volunteer
- Tutored Chinese major students every week.
- Helped their reading, writing, and speaking.

Projects

University of Delaware
Newark, Delaware
2012 – 2016

- Design and Analysis of the Trans-Alaskan and Keystone XL Pipelines
- Investigating the Effects of Atherosclerosis in the Left Coronary Artery Though Computational Fluid Dynamics
- Computer Chip Design Recommendation Using Pin Fin Efficiency Analysis
- Frictional Losses in Pipes and Fittings Developing a Relationship between Design Variables and Pressure Drop
- Determination of Kinetic Parameters Iodination of Acetone
- Optimization of the Biochemical Reactor Design of 1,3-Propanediol
- Production of Green Fluorescent Protein from Escherichia Coli
- Distillation Separation of Water and Methanol
- Hydrogen Oxidation in Presence of Ammonia at Anode in a Hydroxide Exchange Membrane Fuel Cell
- Commercial Production of 3,4-Dichlorobutene